



**HAL**  
open science

## Rotational Modulation of the High Frequency Limit of Saturn Kilometric Radiation

Siyuan Wu, Philippe Zarka, Laurent Lamy, Corentin Louis, Shengyi Ye,  
Renée Prangé, Baptiste Cecconi, William S Kurth

► **To cite this version:**

Siyuan Wu, Philippe Zarka, Laurent Lamy, Corentin Louis, Shengyi Ye, et al.. Rotational Modulation of the High Frequency Limit of Saturn Kilometric Radiation. *Journal of Geophysical Research Space Physics*, 2023, *JGR Space Physics*, 128 (4), 10.1029/2023JA031287 . hal-04090740

**HAL Id: hal-04090740**

**<https://hal.sorbonne-universite.fr/hal-04090740>**

Submitted on 6 May 2023

**HAL** is a multi-disciplinary open access archive for the deposit and dissemination of scientific research documents, whether they are published or not. The documents may come from teaching and research institutions in France or abroad, or from public or private research centers.

L'archive ouverte pluridisciplinaire **HAL**, est destinée au dépôt et à la diffusion de documents scientifiques de niveau recherche, publiés ou non, émanant des établissements d'enseignement et de recherche français ou étrangers, des laboratoires publics ou privés.

# Rotational modulation of the High Frequency Limit of Saturn Kilometric Radiation

Siyuan Wu<sup>1,2</sup>, Philippe Zarka<sup>2\*</sup>, Laurent Lamy<sup>2, 3</sup>, Corentin Louis<sup>4</sup>, Shengyi Ye<sup>1\*</sup>, Renée Prangé<sup>2</sup>, Baptiste Cecconi<sup>2</sup>, William S. Kurth<sup>5</sup>

<sup>1</sup> Department of Earth and Space Sciences, Southern University of Science and Technology, Shenzhen, Guangdong, People's Republic of China

<sup>2</sup> LESIA, Observatoire de Paris, CNRS, Université PSL, Sorbonne Université, Université Paris Cité, CNRS, Meudon, France

<sup>3</sup> Aix-Marseille Université, CNRS, CNES, LAM, Marseille, France

<sup>4</sup> School of Cosmic Physics, DIAS Dunsink Observatory, Dublin Institute for Advanced Studies, Dublin, Ireland

<sup>5</sup> Department of Physics and Astronomy, University of Iowa, Iowa City, IA, USA

Corresponding author: Philippe Zarka ([Philippe.Zarka@obspm.fr](mailto:Philippe.Zarka@obspm.fr)) and Shengyi Ye ([yesy@sustech.edu.cn](mailto:yesy@sustech.edu.cn))

## Key Points:

- The high frequency limit (HFL) of Saturn Kilometric Radiation (SKR) is obtained during the 13-year Cassini mission.
- The average HFL is found to be above and below 600 kHz in the northern and southern hemisphere, respectively.
- A rotational modulation of HFL is verified statistically and by simulation, which excludes a magnetic field anomaly.

## Plain Language Summary

Auroral radio emission from Saturn, namely the Saturn Kilometric Radiation (SKR), is generated along high latitude magnetic field lines via the resonance between energetic electrons and a wave's electric field. The first work on the high frequency limit (HFL) of SKR dates back to 1991. Using data from the Voyager Saturn fly-by, scientists found an asymmetry when the HFL is organized by the longitude of the Sun. Based on this asymmetry, a hypothesis about the existence of a magnetic anomaly in Saturn's magnetic field was proposed, which was a novel and breakthrough discovery at that time, but the later Cassini measurements did not confirm this magnetic anomaly. Cassini's expedition around Saturn with 13-year continuous measurements provided an opportunity to re-study the HFL of SKR. The long-term statistics allow us to exclude the magnetic anomaly hypothesis and instead attribute the asymmetry to a modulation which is introduced by an ionospheric/magnetospheric current system at Saturn. A simulation suggests that both temporal and spatial effects play a role to a certain degree. The average frequency and visibility of the HFL are also discussed. These new results provide new insights into the studies of cyclotron maser-related radio emissions.

37 **Abstract**

38 The high frequency limit (HFL) of the Saturnian Kilometric Radiation (SKR) can probe the deepest  
 39 SKR sources, closest to Saturn's ionosphere. In this study, we determined and analyzed the SKR HFL  
 40 throughout the entire Cassini Saturn orbital tour. The maximum frequency of the northern SKR, whose  
 41 distribution peaks at  $\sim 625$  kHz, is shifted by +100 to +200 kHz from the distribution of southern SKR  
 42 HFL, consistent with the magnetic field offset towards the northern hemisphere at Saturn. The uniformly  
 43 observed SKR HFL in the vicinity of Saturn suggests a broad extent and beaming of the SKR source.  
 44 When the observer is confined to certain locations, the rotational modulation of the SKR HFL is clearly  
 45 observed. This modulation feature of the SKR HFL is statistically established and analyzed in this study.  
 46 The modulation of HFL is best observed at mid-latitudes between  $10^\circ$  and  $40^\circ$  and at almost all local  
 47 times. We perform a simulation that suggests that the modulation of HFL requires the superposition of a  
 48 "clock" like and a rotating source behaviour. By comparing the derived HFL modulation using different  
 49 longitudes with variable and fixed rotation periods, we can exclude the existence of a magnetic anomaly  
 50 that was proposed in a previous study based on the Voyager data. The calculation of the least-square  
 51 periodogram confirms that the modulation observed in HFL is similar to the ones previously detected at  
 52 Saturn.

53 **1. Introduction**

54 Saturn's Kilometric Radiation (SKR) was discovered in the 1980s during the Voyager 1 Saturn  
 55 approach (Kaiser et al., 1980) and was later studied in depth by the Cassini mission (Lamy et al., 2008a,  
 56 2008b; Cecconi et al., 2009; Fischer et al., 2009, see the review of Lamy, 2017 and refs therein). SKR is  
 57 generated along auroral magnetic field lines above Saturn's polar regions via the cyclotron maser  
 58 instability (CMI) (Wu & Lee, 1979; Zarka, 1998; Lamy et al., 2010, 2011, 2018; Mutel et al., 2008;  
 59 Menietti et al., 2011, Treumann, 2006). It is mainly emitted in the free space Right-Hand Extraordinary  
 60 (R-X) mode, which is highly circularly polarized with the wave frequency near the local electron  
 61 cyclotron frequency ( $f_{ce} (Hz) \sim 28 * B (nT)$  with B the local magnetic field), typically ranging from  
 62 a few kilohertz (kHz) to 1 megahertz (MHz). Therefore, higher frequency SKR is generated in the region  
 63 with a stronger magnetic field, i.e., at lower altitudes above the polar regions, if compared to the lower  
 64 frequency SKR sources. SKR sources were first identified by Voyager to reside on the dawnside sector  
 65 of the magnetosphere (Kaiser et al. 1982). The later direction-finding analyses of Cassini measurements  
 66 revealed that SKR sources lie at all longitudes along flux tubes mapping to the main UV auroral oval,  
 67 while being brighter at dawn (Farrell et al., 2005, Cecconi et al., 2009, Lamy et al., 2009, 2011).

68 The CMI-produced emissions are beamed at large angles along the surface of a thin (a few degrees  
 69 wide) hollow cone whose axis is aligned with the local magnetic field in the source (Mutel et al., 2010).  
 70 This beaming pattern is responsible for a highly anisotropic emission with strong visibility effects, so the  
 71 observed SKR time-frequency features highly depend on the observers' location (Lamy et al., 2008b,  
 72 2013, Cecconi et al., 2009). Because the magnetic field directions in the two hemispheres are opposite,  
 73 the R-X mode emissions with right-hand polarization with respect to the magnetic field direction would  
 74 show two different circular polarization senses in the data-derived Stokes parameter related to either  
 75 north or south. The SKR observed at high latitudes exhibits circular polarization, either  $>0$  (in the south)  
 76 or  $<0$  (in the north), whereas a superposition of the north and south SKR at the low latitude region  
 77 produces a very complicated polarization pattern.

78 SKR activity has been studied and linked to magnetospheric dynamics (Kurth et al., 2005; Jackman  
 79 et al., 2010; Lamy et al., 2013). The SKR radiated power is strongly correlated with the solar wind  
 80 dynamic pressure fluctuations (Desch, 1982; Desch & Rucker, 1983; Jackman et al., 2010; Taubenschuss

81 et al., 2006; Zarka et al., 2007). The Low-Frequency Extensions (LFE) of SKR have been used as a proxy  
 82 for reconnection events and compression-induced hot plasma injections (Bunce et al., 2005; Jackman &  
 83 Arridge, 2011; Jackman et al., 2009, 2010; Reed et al., 2018). The high frequency limit (HFL) of SKR  
 84 was also found to be linked mainly to the solar wind dynamics near Saturn, but also to the rotation of the  
 85 planet (Saturn's longitude) (Galopeau, Ortega-Molina, and Zarka, 1991; Galopeau and Zarka, 1992).  
 86 While SKR maximal frequencies were measured as high as 1200 kHz using Voyager observations  
 87 (Kaiser et al., 1980), they remained generally below 1000 kHz when measured from Cassini, with a  
 88 50-100 kHz offset of the northern SKR relative to the southern SKR (Lamy et al., 2008a). Long-term  
 89 variations of the SKR northern and southern maximal frequencies were tested and no relation between  
 90 the maximal frequency and the solar wind or solar EUV flux was found (Kimura et al., 2013).

91 The SKR HFL was studied earlier using the data obtained during the Voyager 1&2 Saturn fly-bys. A  
 92 sinusoidal variation was observed when the HFL was organized as a function of the sub-solar longitude  
 93 (Galopeau, Ortega-Molina, and Zarka, 1991; Galopeau and Zarka, 1992). This asymmetry was  
 94 tentatively explained by non-axisymmetric high-order terms in the spherical harmonics decomposition of  
 95 Saturn's magnetic field, mainly resulting in a magnetic anomaly in Saturn's northern hemisphere. Indeed,  
 96 for a source fixed in local time (LT) as was thought to be the case for the SKR in the 1990s (Warwick et  
 97 al., 1981), a rotating magnetic anomaly would cause a periodic variation of  $f_{ce}$  in the source while the  
 98 plasma frequency ( $f_{pe}$ ) remains constant to first order, leading to a periodic variation of the SKR HFL  
 99 with the sub-solar longitude (i.e., with the rotation of the planet), as explained in Fig. 4 of Galopeau,  
 100 Ortega-Molina, and Zarka (1991). During the Cassini era, the subsequent in-situ magnetic field  
 101 measurements obtained above the northern auroral region did not confirm the presence of such an  
 102 anomaly (Cao et al., 2011, 2020; Dougherty et al., 2018). The importance of the SKR HFL comes from  
 103 the fact that it reflects the characteristics of the SKR source regions closest to Saturn, hence probing the  
 104 high-order terms of the magnetic field and the upper ionosphere. Long-term measurements recorded  
 105 during the Cassini tour offer the unique possibility to explore further the characteristics of the SKR HFL  
 106 well beyond the brief Voyager measurements (3-4 months for each fly-by). This work analyzes the SKR  
 107 HFL obtained from the Cassini radio data during its 13 years in orbit around Saturn. The data and the  
 108 algorithm developed to find the HFL are described in Section 2. We discuss the observed characteristics  
 109 of HFL (N/S asymmetry, global distribution, and longitudinal modulation) in Sections 3-6. We compare  
 110 them to simulations of the SKR visibility in Section 7 and we summarize our results in Section 8.

## 111 2. Data and Method

112 The High Frequency Receiver (HFR) of the Radio and Plasma Wave Science (RPWS) instrument  
 113 onboard Cassini measured the radio wave electric field from 3.5 kHz to 16.125 MHz (Gurnett et al.,  
 114 2004). SKR usually covers a broad frequency range, from a few kHz to around one MHz (Kaiser et al.,  
 115 1980; Lamy et al., 2008a; Kimura et al., 2013). In this work, we analyze the electric field spectrograms  
 116 over frequencies ranging from 200 kHz to 1300 kHz and from 2004 day 001 (day of year) to 2017 day  
 117 258. The wave polarization data (Stokes V, i.e., circular polarization degree, Kraus, 1986) used in this  
 118 study are obtained from the goniopolarimetric inversion of auto- and cross-correlations of RPWS  
 119 antenna signals (Cecconi & Zarka, 2005) under the assumptions that either:

- 120 (1) The emissions originate from the centre of Saturn; this inversion produces the so-called n3d level  
 121 data (Cecconi, Lamy, and Zarka, 2017a), or
- 122 (2) The emissions are purely circularly polarized, with linear polarization parameters  $Q=U=0$ ; this  
 123 inversion produces the n3e level data (Cecconi, Lamy, and Zarka, 2017b). Under this assumption, the

124 derived circular polarization can also be less than 1 ( $|V| < 1$ ), because of a lower degree of total  
125 polarization.

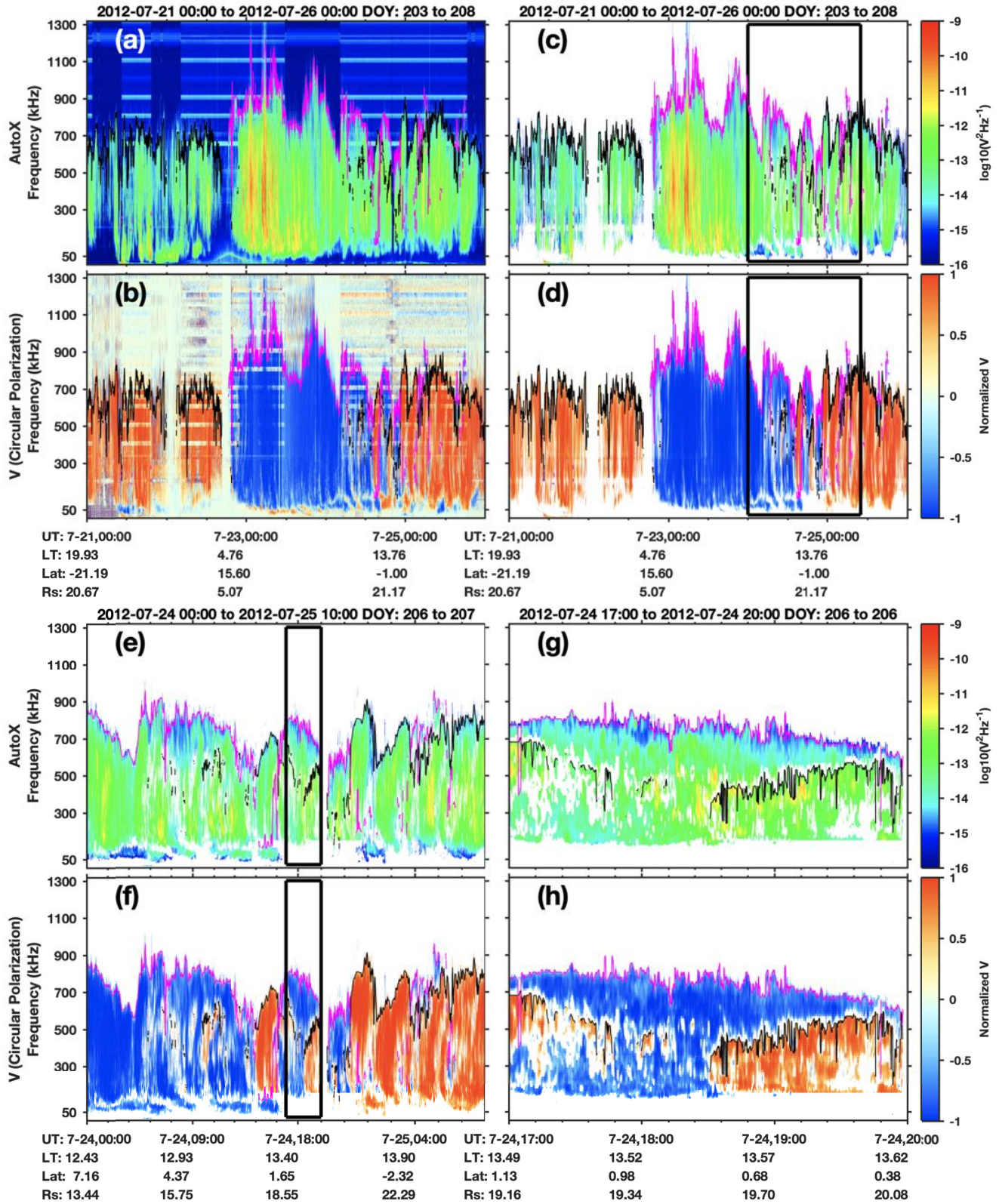
126 To find the SKR HFL, we first eliminate the unwanted data (e.g., instrumental interference,  
127 harmonics of SKR (Wu et al., 2022a)) in the wave intensity and polarization spectrograms. For that  
128 purpose, we apply the selection criteria below:

- 129 (1) Data points with circular polarization (Stokes V in both n3e and n3d data) value  $\text{abs}(V_{n3e}) < 0.3$   
130 and  $\text{abs}(V_{n3d}) < 0.3$  are deleted from the intensity and circular polarization spectrograms.
- 131 (2) Data points with intensity  $< 10$  dB are deleted (in n3e and n3d data) from the intensity and circular  
132 polarization spectrograms.

133 Secondly, to mitigate the contamination from low-frequency O mode emissions, e.g., Saturn  
134 narrowband emissions (mostly below 70 kHz and mainly near 5 and 20 kHz, Ye et al., 2009; Wu et al.,  
135 2021), Saturn Anomalous Myriametric radiation (below 30 kHz, Wu et al., 2022b), and the O mode SKR  
136 (below 100 kHz, Lamy et al., 2008a), which are superimposed and mixed with the SKR emissions from  
137 time to time, we eliminate the data with frequencies below 200 kHz. Because the O mode SKR emissions  
138 are only marginally observed with weaker intensity and the occurrence is relatively rare (Lamy et al.,  
139 2008a), the possible high frequency O mode SKR emissions are simply ignored.

140 A 2-D median filter (with  $3 \times 3$  channels in the time-frequency plane) is then applied to the  
141 processed intensity and circular polarization spectrograms to eliminate isolated emission pixels. Finally,  
142 we find the maximum frequency of both the right-hand and left-hand polarized SKR waves at each time  
143 step. The data point identified as the maximum frequency should satisfy that: (1) intensity  $> 20$  dB, (2)  
144 circular polarization ( $\text{abs}(V)) > 0.3$ , (3) intensities are continuous below the maximum frequency for at  
145 least 4 adjacent frequency channels.

146



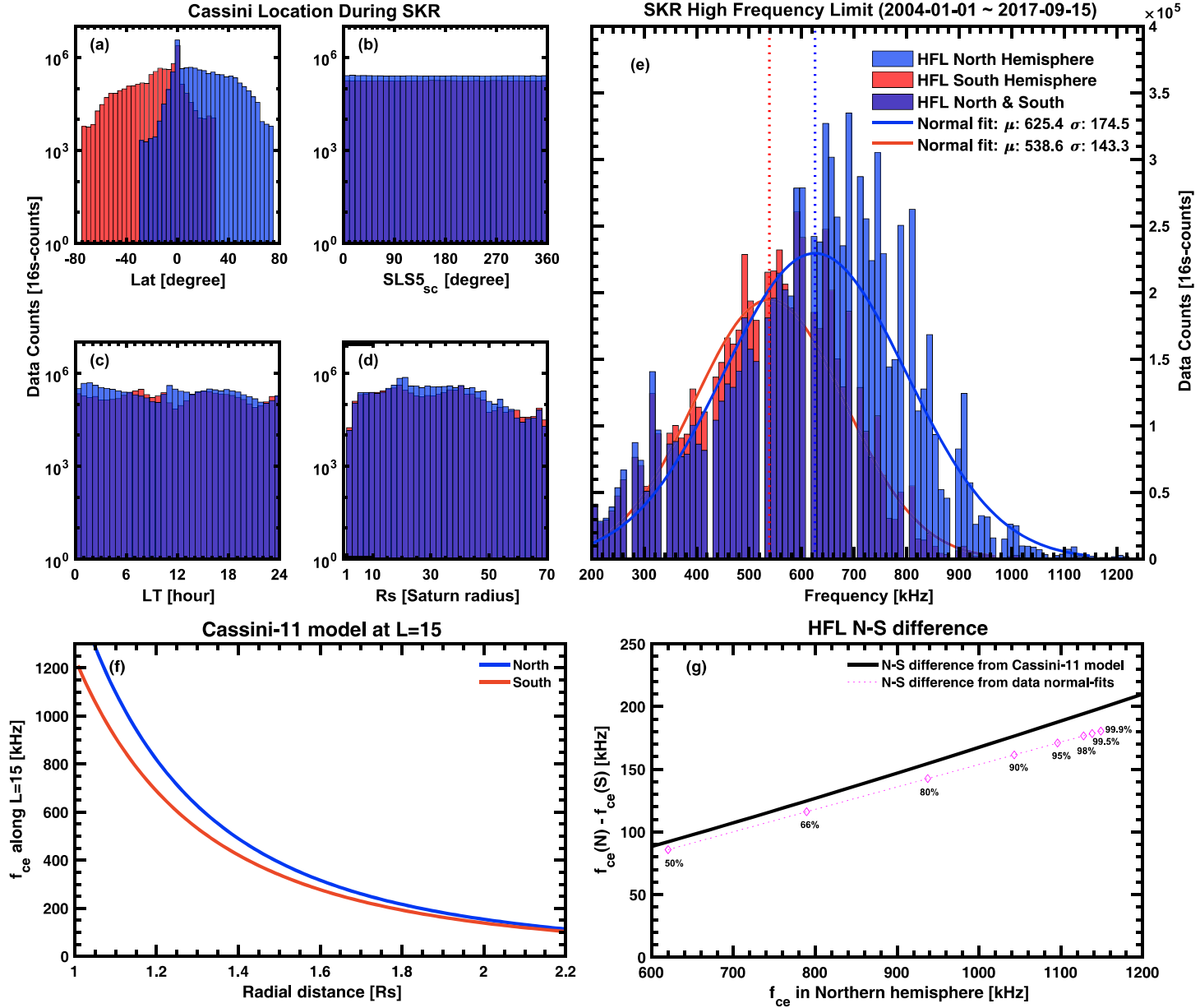
147

148 **Figure 1.** Examples of the identified SKR HFL. Panels (a)-(b) display the RPWS electric field intensity  
 149 spectrogram and the circular polarization (n3d level data, obtained from the inversion method of Cecconi  
 150 and Zarka (2005)) over a duration of 5 days. Panels (c)-(d) show the corresponding processed data over

151 the same interval as Panels (a)-(b). Panels (e)-(f) zoom into the black box of Panels (c)-(d) over a  
152 duration of 34 hours. Panels (g)-(h) zoom into the black box of Panels (e)-(f) over a duration of 3 hours.  
153 The superimposed pink and black lines mark the identified HFL of the SKR emissions based on the  
154 polarization sense, with pink for right-hand and black for left-hand.

155 The example in Figure 1 illustrates the performance efficiency of the selection criteria in finding  
156 the SKR HFL. The unprocessed wave electric field intensity and circular polarization spectrograms from  
157 2012-07-21 to 2012-07-26 are shown in Figure 1 Panels (a)-(b). The processed data and the zoom-in  
158 results are given in Panels (c)-(d) and Panels (e)-(h). The overlapped pink and black lines mark the SKR  
159 HFL found for the right-hand and left-hand polarized waves, respectively. The obtained HFL lines are  
160 well aligned on the top of the SKR emission, suggesting that the algorithm is good enough to capture the  
161 temporal variations of the SKR HFL. At low latitudes, the north and south SKR are overlaid together as  
162 shown in Figure 1 Panels (f) and (h). The algorithm can pick up both the north and south SKR at each  
163 time step according to the polarization sense, e.g., at 07-24 19:00 in Panel (h). Because at low latitudes  
164 the lower HFLs from one hemisphere may be polluted by the superposition effect of emissions from the  
165 other hemisphere, only the higher HFL is kept at each time step. Finally, 9147518 (~4.64 years) and  
166 6957390 (~3.53 years) HFL values were obtained for the north and south, respectively. The time  
167 resolution of the RPWS data is typically 16s and depends on the operation mode of the receiver.

### 168 **3. The North-South Asymmetry of the SKR HFL**



169

170 **Figure 2.** North-South asymmetry of the SKR HFL distributions. Panels (a)-(d): Positions of Cassini  
 171 during the observation of SKR HFL with (a): Latitude, (b): Longitude of Cassini, derived from the SLS5  
 172 system (Ye et al., 2018), (c) Local time, (d) Radial distance. Panel (e): Histogram of the identified SKR  
 173 HFL with normal fits superimposed. The blue and red bins represent the observations of north and south  
 174 SKR, respectively. The dark blue color indicates regions with an HFL from both northern and southern  
 175 SKR (the overlap of light blue and red bars). Panel (f): The  $f_{ce}$  values as a function of radial distance  
 176 calculated using the Cassini-11 magnetic field model (Dougherty et al., 2018) at Lshell=15. The north  $f_{ce}$   
 177 (blue line) is larger than the south  $f_{ce}$  (red line) due to the northward offset of the magnetic field at Saturn.  
 178 Panel (g): Calculated difference  $f_{ce}(r)_{\text{North}} - f_{ce}(r)_{\text{South}}$  (solid black line) is plotted versus the northern  $f_{ce}$ ,  
 179 and compared with that derived from the model fits in Panel (e) (pink dashed line and diamonds). The  
 180 pink diamonds (frequency differences) are taken at the same percentile from the two curves in Panel (e).  
 181 The good match confirms that the N-S difference in the HFL is generated by the offset of Saturn's  
 182 magnetic field.



183 The average frequency of the north and south SKR HFL are estimated in Figure 2. To check any  
 184 possible bias caused by the anisotropic beaming pattern of SKR and the observing geometry of Cassini  
 185 (Lamy et al., 2008a, 2008b, 2013), the positions of Cassini when the SKR HFL are identified are plotted  
 186 in Figure 2, Panels (a)-(d). The observation positions of Cassini for all Saturn orbits during the 13  
 187 year-tour are almost symmetric in the northern and southern hemispheres, which allows us to exclude the  
 188 uncertainty caused by the geometry effects in estimating the average frequency. The longitude of Cassini  
 189 used in Panel (b) is derived from the Saturn Longitude System 5 (SLS5, Ye et al., 2018,  $\lambda_{sc} =$   
 190  $\lambda_{sun} + (12 - LT_{sc}) * 15^\circ$ ,  $\lambda_{sc}$  is the longitude of the spacecraft,  $\lambda_{sun}$  is the longitude of the sun,  $LT_{sc}$  is the  
 191 spacecraft local time). Because Cassini was inserted in Saturn's orbit from the southern hemisphere in  
 192 2004 along orbits with apokrones in the southern hemisphere in the first year of the tour, there is a slight  
 193 excess of observations of the southern SKR HFL at larger radial distances (not shown), e.g., with radial  
 194 distance  $> 70$  Rs (Saturn Radius=60268 km). This is a source of bias for the southern HFL at the larger  
 195 radial distance, and therefore we remove long distance ( $>70$  Rs) observations to eliminate the possible  
 196 bias in the estimation of the average frequency.

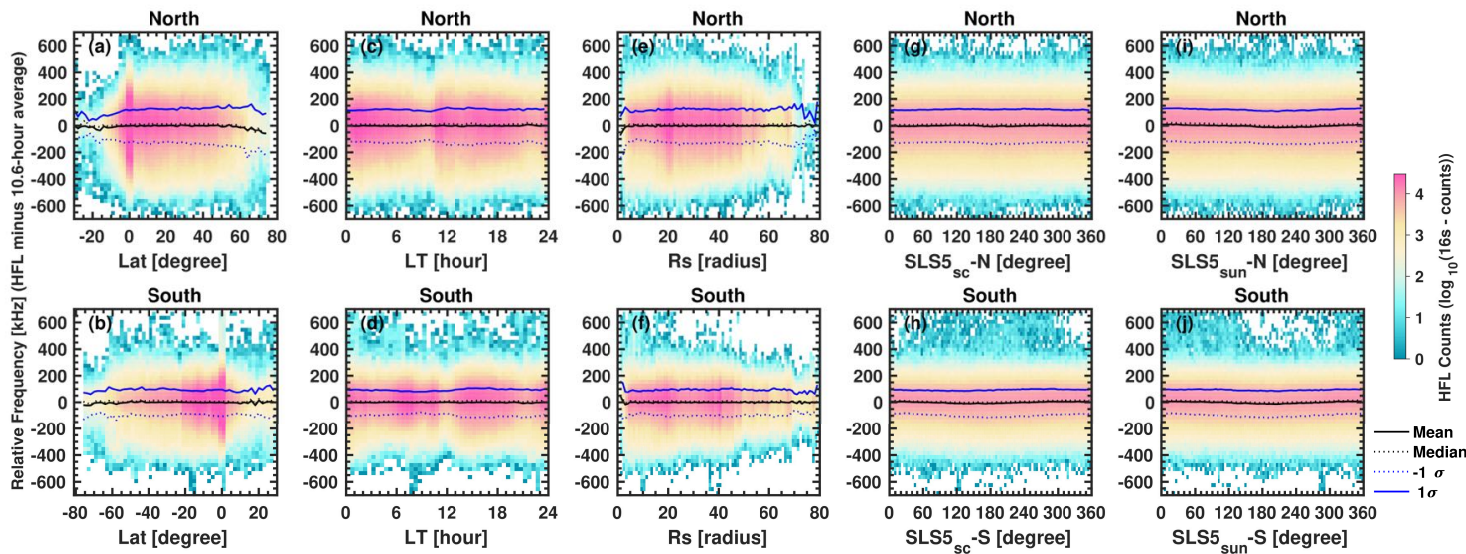
197 The fitted average SKR HFL frequencies of the north ( $\sim 625$  kHz) and south ( $\sim 539$  kHz) are  
 198 estimated using normal (Gaussian) fits of the histograms in Figure 2 Panel (e). Note here that the shapes  
 199 of the histograms in Panel (e) do not fully represent the characteristics of normal distributions, which  
 200 causes uncertainties for derived average HFL values. However, this rough estimation is sufficient to  
 201 draw conclusions. The  $\sim 87$  kHz difference in frequency is consistent with the previous results of a  
 202 50-100 kHz range in Lamy et al. (2008a), as previously computed over a more restricted time interval  
 203 that was proposed to result from the  $\sim 0.0466$  Rs northward offset of the kronian magnetic field (Lamy et  
 204 al. 2008a). As SKR is produced close to the local  $f_{ce}$  (Lamy et al., 2018), directly proportional to the local  
 205 magnetic field, the higher average frequency HFL in the north implies that the source region of the  
 206 northern SKR lies in a position with a stronger magnetic field than the southern SKR source region. The  
 207 "minimum altitude" of SKR source is primarily determined by the density depletion in the ionosphere  
 208 and it should be similar in both hemispheres, one can expect similar altitudes of northern and southern  
 209 SKR sources above the surface of Saturn, because particle densities in the ionosphere rather depend on  
 210 the gravity field and not on the magnetic field.

211 Consequently, the explanation of the north-south differences in the average HFL resides in the  
 212 northward offset of Saturn's magnetic field (the magnetic equator is shifted northward from the  
 213 planetographic equator by  $\sim 0.0466$  Rs (Dougherty et al., 2018). Using the Cassini-11 magnetic field  
 214 model (Dougherty et al., 2018),  $f_{ce}$  values along a typical SKR L-shell ( $L=15$ , corresponds to invariant  
 215 latitude =  $75^\circ$ ) were calculated and plotted versus the radial distance in both hemispheres in Figure 2  
 216 Panel (f). The L-Shell (McIlwain, 1966) corresponds to the distance (normalized to planetary radius) of a  
 217 dipolar field line apex in the equatorial plane. The calculated  $f_{ce}$  in the northern hemisphere is larger than  
 218 in the southern hemisphere at the same altitudes, and the difference becomes larger at smaller radial  
 219 distances, which is because the magnetic field decays with the cube of the radial distance. This feature  
 220 implies that the North-South differences in the HFL will also increase as the HFL increases. A  
 221 comparison is given in Panel (g), where the calculated difference  $f_{ce}(r)_{North} - f_{ce}(r)_{South}$  from the Cassini-11  
 222 model is plotted versus the northern  $f_{ce}$  (solid black line), and compared with that measured from the  
 223 normal fits in Panel (e) (pink dashed line with diamonds). The solid black line is directly calculated using  
 224 the two lines in Panel (f). The pink dashed line with diamonds is calculated using the two normal fits in  
 225 Panel (e), e.g., the peak-peak frequency difference (difference of 50% - 50% percentile values for the two  
 226 distributions) is 625.4 kHz - 538.6 kHz  $\sim 87$  kHz as indicated by the vertical dashed lines in Panel (e).  
 227 The percentile values (at 50%, 66%, 80%, 90%, 95%, 98%, 99.5%, 99.9%) of the two normal fits in the  
 228 two distributions are measured and the corresponding frequency differences are plotted in Panel (g) as

229 the diamonds. The two lines deviate from each other slightly at high frequencies. This is likely due to the  
 230 fewer data points for HFL at high frequencies and the uncertainty on the normal distribution fits. The  
 231 good match between the solid black line and the pink dashed line confirms that the magnetic field offset  
 232 is responsible for the observed difference in the northern and southern SKR HFL.

233 Another interesting point here is the spread of HFL (sigma values in Figure 2 Panel (e)). The  
 234 frequency variations in HFL as large as  $\sim 400$  kHz could be related to solar wind dynamics as suggested  
 235 by previous studies (Galopeau, Ortega-Molina, and Zarka, 1991; Taubenschuss et al., 2006), similar to  
 236 the LFE at Saturn (Jackman et al., 2009; Reed et al., 2018). The link between the High-Frequency  
 237 Extensions (HFE) of SKR and their connection to the solar wind dynamics would be worth a future  
 238 study.

#### 239 4. The spatial visibility of the relative SKR HFL



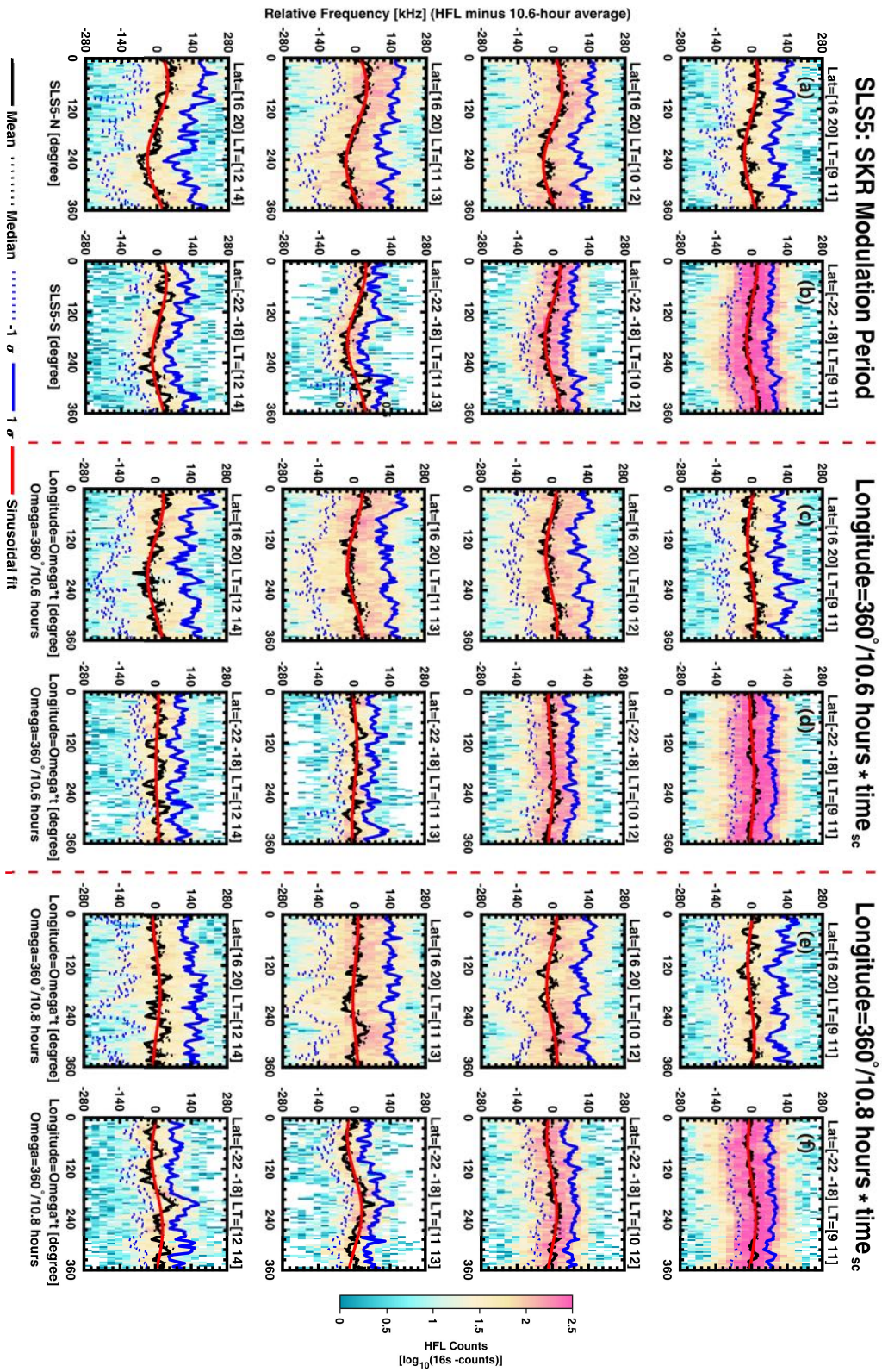
240

241 **Figure 3.** Distributions of the relative HFL. The quantity shown along the y-axis is the relative HFL, i.e.,  
 242 the instantaneous – rotation-averaged HFL. Panels (a)-(b) show the relative HFL distributions in latitude,  
 243 separately for the northern and southern hemisphere. Panels (c)-(d) and (e)-(f) are the distributions of  
 244 relative HFL vs local time and radial distance. Panels (g)-(h) and (i)-(j) are the distributions of relative  
 245 HFL in SLS5 longitude system, using different longitude frames: spacecraft SLS5 in Panels (g)-(h) and  
 246 sub-solar SLS5 in Panels (i)-(j). The black lines mark the mean (solid) and the median (dashed, nearly  
 247 superimposed to the mean) relative HFL derived from data with abscissa in the corresponding bin. The  
 248 blue lines give the  $+1\sigma$  (solid) and  $-1\sigma$  (dashed) extent of the relative HFL distribution at each abscissa.

249 The distributions of the relative SKR HFL are overplotted in Figure 3 as a function of the location of  
 250 Cassini (in Latitude, Local Time, Radial distance, and Longitude in Panels (a)-(b), (c)-(d), (e)-(f) and  
 251 (g)-(h)). To eliminate long period, externally-controlled variations of the HFL, e.g., due to the solar wind  
 252 (Galopeau, Ortega-Molina, and Zarka, 1991; Galopeau and Zarka, 1992), a 10.6 hour (1 Saturn rotation  
 253 period) running-average was subtracted from the instantaneous HFL. The calculated mean, median and  
 254  $\pm 1$  sigma values of the corresponding relative HFL distributions are overlapped as solid and dashed lines  
 255 in each panel. Exploring the relative HFL distribution along a single spatial parameter is not rewarding  
 256 due to the anisotropic beaming of SKR, which couples the different spatial parameters.

257 All means and medians are flat and close to zero as indicated by the black lines in Figure 3,  
258 confirming the absence of bias and suggesting that the beaming of SKR beam statistically covers all  
259 spatial regions around Saturn. No particular position is found for which the absolute HFL would be  
260 predominantly above or below the 10.6-hour running average. In Panels (a)-(b), more counts are  
261 observed at low latitudes (the reddish peak near  $0^\circ$ ) because Cassini spent a long time in the equatorial  
262 region, but without changing the mean or median. The fewer points of HFL above 60 degrees in latitude  
263 in Panels (a)-(b) are because most SKR emissions are observed below 60 degrees. There are also fewer  
264 HFL observed beyond a distance of  $\sim 50$  Saturn radii in Panels (e)-(f), which is due to the fact that Cassini  
265 spent most of its time within 50 Saturn radii. There are more points around 20 Saturn radii, because  
266 Cassini also spent a long time there, mainly during the numerous Titan fly-bys. Note here that the  
267 standard deviations of the relative HFL are always slightly higher in the northern hemisphere than in the  
268 southern hemisphere (for all 5 displayed coordinates), which agrees with the general normal fits for north  
269 & south HFL in Figure 2 Panel (e). We also organized the relative HFL as a function of sub-solar  
270 longitude in Panels (i)-(j) for a first check of a possible asymmetry like the one found in Voyager data  
271 (Galopeau, Ortega-Molina, and Zarka, 1991). No such asymmetry is observed. But as 13-year statistics  
272 may smooth any asymmetry, we further explore these distributions by restricting the Cassini location to  
273 small (LT, latitude) intervals, as discussed in the next Section.

## 274 **5. The longitudinal modulation of the relative SKR HFL**



276 **Figure 4.** Examples of longitudinal modulation of the relative SKR HFL. Columns (a)-(b), Examples of  
 277 the longitudinal modulation of relative SKR HFL observed in the northern and southern hemispheres.  
 278 Different sub-panels give observations at various (Latitude, LT) positions of Cassini. The black lines  
 279 show the mean (solid) and median (dashed, hardly visible) relative HFL versus sub-solar longitude  
 280 (SLS5, Ye et al., 2018). The red lines are the sinusoidal fits of the solid black lines.  $+1\sigma$  and  $-1\sigma$  width of  
 281 the relative HFL distribution at each abscissa are plotted by solid and dashed blue lines, respectively.  
 282 Columns (c)-(d) and (e)-(f) repeat the analysis from Columns (a)-(b) but using different longitude  
 283 systems, derived from different tentative rigid rotation periods of Saturn, 10.6 hours in Columns (c)-(d)  
 284 and 10.8 hours in Columns (e)-(f).

285 We restrict the location of Cassini to small spatial bins in local time and latitude ( $4^\circ$  Lat  $\times$  2 hours  
 286 LT) to further explore the relative HFL variation as a function of sub-solar longitude. The SLS5  
 287 longitude system used in this work is derived from the long-term tracking of average SKR peak  
 288 intensities. The zero degree of sub-solar longitude in SLS5 corresponds to the maxima of SKR intensity,  
 289 which usually peaks on the morning side (Ye et al., 2018; Lamy et al., 2009). The SLS5 system follows  
 290 two time-variable periods, one per hemisphere, clearly distinct ( $\sim 10.6$  h and  $\sim 10.8$  h) from 2004 until the  
 291 end of 2008 (Gurnett et al., 2009). The two periods started to converge around the vernal equinox of  
 292 Saturn in 2009 and crossed each other briefly in late 2009 before starting to oscillate around 10.7 h for  
 293 four years. The southern period remained at 10.7 h until the end of the mission, whereas the northern  
 294 period slowed down in 2014 and 2015 to end up at  $\sim 10.8$  h for the last two years until September 2017  
 295 (see the introduction of Ye et al., 2018). The SKR-intensity derived SLS5 naturally contains information  
 296 on the modulation of SKR generation, which is further related to the modulation of a field-aligned  
 297 current system at Saturn (Southwood and Cowley, 2014; Provan et al., 2018). When confining the  
 298 observer to particular LT bins, the sub-solar longitude is related to the spacecraft longitude via a simple  
 299 shift ( $\lambda_{sc} = \lambda_{sun} + (12 - LT_{sc}) \times 15^\circ$ ). The relative HFL observed from a fixed location is then stacked  
 300 and binned as a function of sub-solar longitude. This procedure allows us to exclude the effects of  
 301 observation geometry and to mitigate the effect of the SKR beaming.

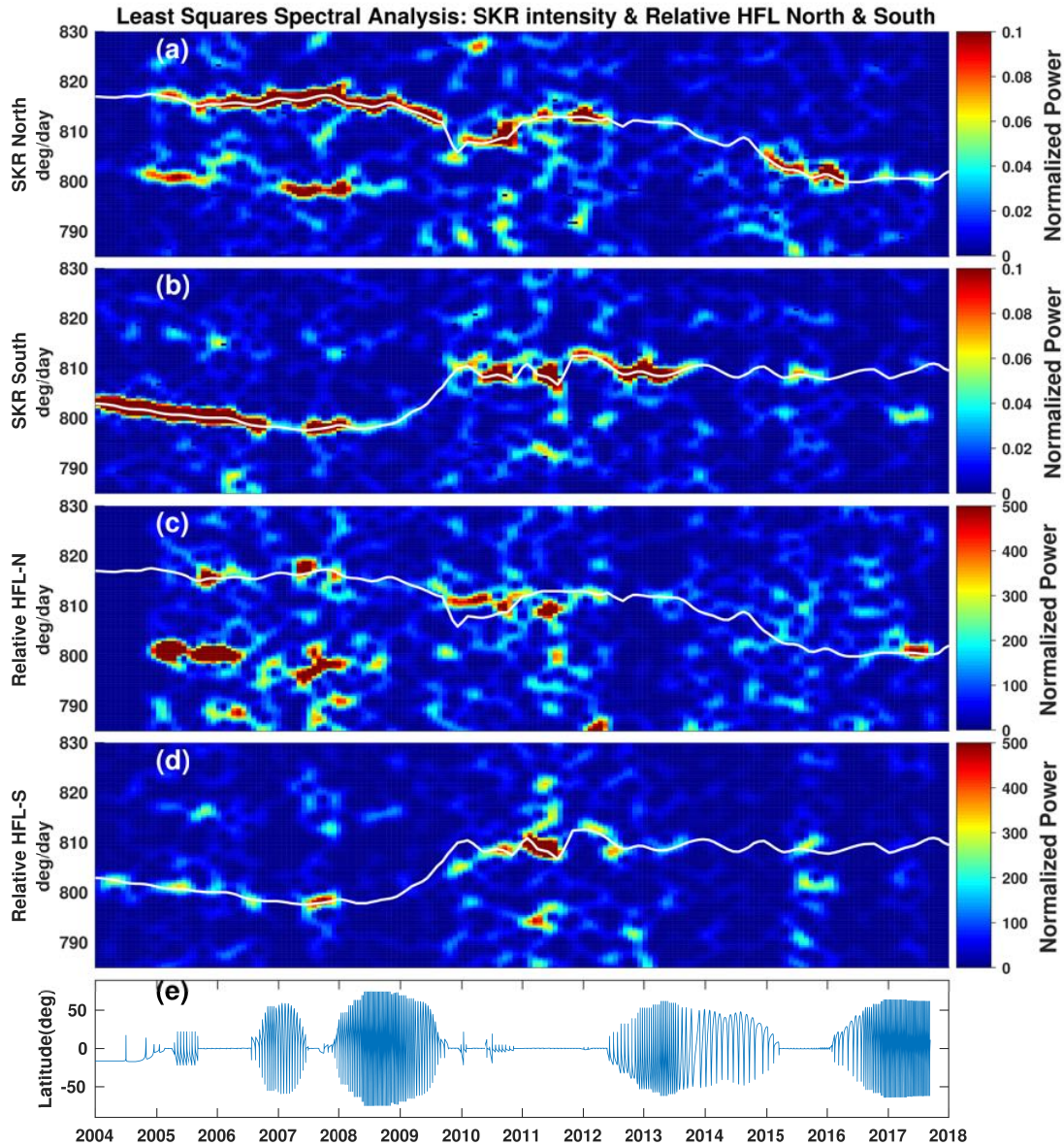
302 As shown by the averaged relative HFL (solid black lines) in Figure 4 Columns (a)-(b), the mean  
 303 relative HFL shows regular quasi-sinusoidal variations as observed from the different locations in local  
 304 time (different sub-Panels) in both hemispheres. A sinusoidal fit (red lines in Figure 4,  $A *$   
 305  $\sin(\lambda_{sun} + \varphi) + offset$ ,  $A$ : amplitude,  $\varphi$ : phase) is computed for the variations of the average relative  
 306 HFL in each spatial bin. Broad enough bins in local time (2 hours) and latitude (4 degrees) are needed to  
 307 gather enough data points in each bin and thus guarantee the accuracy of the calculation of the average  
 308 relative HFL. In each spatial bin, we require that relative HFL data represent an observation time larger  
 309 than three Saturn rotation periods (thus  $\sim 32$  hours). The observation time for each bin is given in Figure  
 310 A1 in the Appendix. To increase the resolution of the sinusoidal fit, there is a 50% overlap between  
 311 consecutive bins (i.e., 1 hour steps in LT and 2 degrees in latitude), leading to a total of 816 spatial bins.  
 312 For the sinusoidal fit in each spatial bin, the root mean square deviation (RMSD) is used to measure the  
 313 fit quality and discard the poor fits (that correspond to  $RMSD > 0.1$ ;  $\sim 40\%$  of the fits have RMSD larger  
 314 than 0.1; see their distribution in Figure A1).

315 The sinusoidal variations of relative HFL observed in some bins are reminiscent of the first  
 316 results from Galopeau, Ortega-Molina, and Zarka, (1991), which was tentatively explained by the  
 317 presence of a magnetic anomaly. However, in our case the relative HFL is organized as a function of  
 318 SLS5, which is not related to the rotation of the planet but to that of a particular current system (Ye et al.,  
 319 2018; Andrews et al., 2011; Cowley and Provan, 2017). To give an intuitive illustration of the SKR  
 320 intensity and HFL modulation with SLS5, an example is given in Figure A2. The recurring emission

321 occurrence peaks on the spectrum in Figure A2 show the characteristic SKR periodic modulation. The  
322 pink lines on top of the SKR emission, as well as the relative HFL in Figure A2 Panel (d), indicate that  
323 the HFL & relative HFL also experience a modulation that mirrors the repetition of the SKR emission  
324 occurrence peaks.

325 To explore further whether this modulation in relative HFL could reveal a magnetic anomaly or is  
326 controlled by the SLS5 modulation, the relative HFL are further organized by using a series of longitude  
327 systems derived assuming fixed rotation periods. For example, in Figure 4 Columns (c)-(d) and (e)-(f)  
328 10.6 hours and 10.8 hours rotation periods are adopted. Should this variation be generated due to a  
329 magnetic anomaly that corotates with the planetary magnetic field, the longitude derived using a fixed  
330 rotation period should better organize the variation in relative HFL. As can be seen from Figure 4  
331 Columns (c)-(d) and (e)-(f), weaker amplitudes or even lack of modulation are observed when the  
332 relative HFL are organized in fixed-period longitude systems. All rotation periods from 10.5 to 11 hours  
333 by step of 0.1 hour were also tested (not shown), but none led to a relative HFL longitudinal modulation  
334 better organized (i.e. deeper) than the one obtained with SLS5.

335 For confirmation, a Least-Square-Spectrum-Analysis (LSSA) periodogram was built using the  
336 relative HFL series obtained in this study, which is presented in Figure 5. The LSSA, also known as  
337 Lomb-Scargle analysis (Lomb, 1976; Scargle, 1982), is a method for estimating the time-frequency  
338 spectrum of a time series, which is particularly suitable for the analysis of unevenly sampled data with  
339 gaps. The LSSA parameters used to produce Figure 5 are the same as those adopted by Ye et al. (2018).  
340 For more information about the LSSA method, readers are referred to Ye et al. (2016, 2018) and Gurnett  
341 et al. (2009).



342

343 **Figure 5.** LSSA spectrograms of SKR and relative SKR HFL from 2004 to 2018. The color-coded  
 344 spectrograms represent the modulation power as a function of universal time on the horizontal axis and  
 345 modulation rate on the vertical axis. Panels (a)-(d) show the results for the north hemisphere SKR  
 346 intensity, south hemisphere SKR intensity, north hemisphere relative SKR HFL, and south hemisphere  
 347 relative SKR HFL, respectively. Panel (e) displays the Cassini latitude during the Saturn orbital tour. The  
 348 white lines in the four panels represent the northern and southern SKR periods, as derived by Ye et al.  
 349 (2018). The white lines in Panels (a) and (c) are the same for the north hemisphere SKR, while the white  
 350 lines in Panels (b) and (d) are the same for the south hemisphere SKR. The relative HFL in Panels (c)-(d)  
 351 is obtained by subtracting two rotation period average values from the absolute HFL, i.e., instantaneous –  
 352 2-rotation-period-averaged HFL.

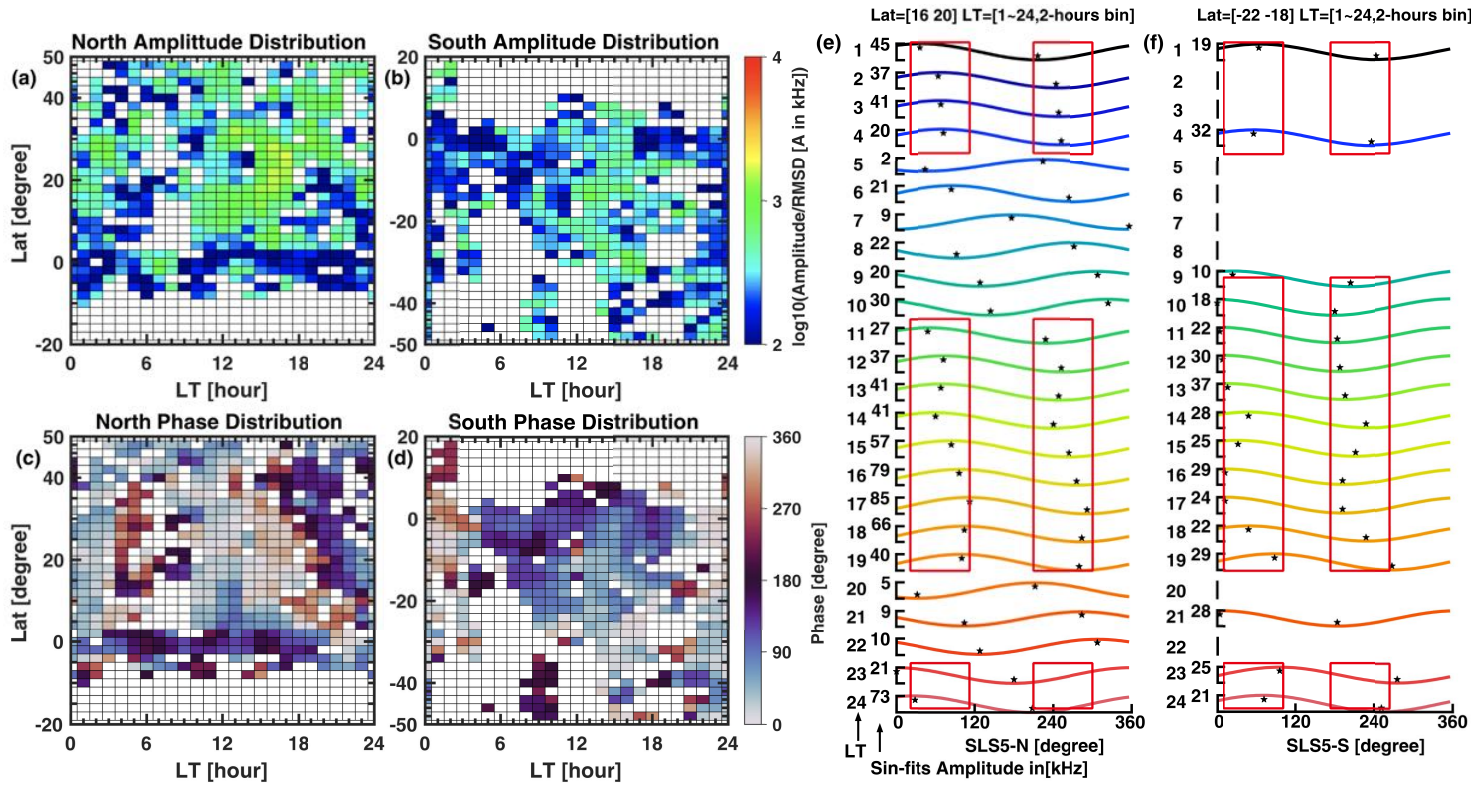
353 Panels (a) and (b) of Figure 5 are the SKR intensity modulation spectrograms reproduced from  
 354 Figure 1 of Ye et al. (2018). The well-known modulation of SKR intensity reveals two distinct periods  
 355 near 10.6 hours and 10.8 hours for the north and south hemispheres, respectively, and the merging and

356 reversal. The white lines mark the SKR rotational modulation rates for the north in Panel (a) and the  
357 south in Panel (b). Panels (c) and (d) show the results of the calculations using the relative HFL time  
358 series obtained in this work. The relative HFL series used here are adapted by subtracting the  
359 running-mean values of two rotation periods from the absolute HFL values. This was done to mitigate  
360 possible bias caused by the process of subtracting one rotation period, as the modulation periods are close  
361 to one Saturn rotation period of 10.6 hours. One can easily recognize similar modulation features  
362 between the SKR intensity and the relative SKR HFL by comparing Panels (a) and (c), and Panels (b) and  
363 (d). Note that the integrated SKR intensities in Panels (a)-(b) are obtained by dividing one rotation period  
364 average values from the integrated intensities according to the previous work (Ye et al., 2016; 2018;  
365 Gurnett et al., 2009). Therefore, the values of the normalized modulation power in Panels (a)-(b) are  
366 smaller, whereas the normalized modulation power in Panels (c)-(d) is larger due to the subtracting  
367 process. This calculation directly confirms the modulation of HFL with variable periods and excludes the  
368 possibility of constant period modulation or the existence of a magnetic anomaly.

369 It is interesting to note that the northern SKR (Figure 5 Panels (a) and (c)) also has a second period  
370 from early 2005 to the end of 2009 of around 800 deg/day, which is the same period as that of the  
371 southern SKR. This might either result from an incorrect separation of northern and southern sources, or  
372 electron populations from the south bounce to the north, where they also generate northern SKR with the  
373 southern period as suggested by Hunt et al. (2015) and Kivelson and Jia. (2017). It is worth noting that  
374 this secondary period of northern SKR at 800 deg/day seems to have a larger modulation signal as the  
375 primary northern period around 820 deg/day in the rotational analysis of the relative HFL. Furthermore,  
376 there is some deviation in the northern period calculated from the SKR intensity (white line) compared to  
377 the result from the relative SKR HFL, and the first deviation can be seen in Panel (c) in the time interval  
378 from Saturn equinox (August 2009) until mid-2010. There the relative HFL modulation signal slightly  
379 above 810 deg/day is about 3 deg/day higher than the white line. The second deviation occurs during the  
380 year 2011, where the rotation of the northern SKR intensity denoted by the white line is about 3 deg/day  
381 quicker than the northern HFL modulation signal. This second deviation could be caused by the intense  
382 secondary signal from southern hemisphere, but this is not the case for the first deviation. The differences  
383 between the SKR modulation period and the one derived from the magnetic field from 2009-2013 were  
384 discussed in Fischer et al. (2015), and the relative HFL modulation signal slightly above 810 deg/day  
385 from equinox to mid-2010 rather agrees with the period derived from the magnetic field (Cowley and  
386 Provan 2016). Other than that, the modulation features between the relative SKR HFL and the SLS5 are  
387 quite similar.

## 388 **6. The distribution and phase of the relative HFL modulation features**





389

390 **Figure 6.** Distribution of the modulation of relative SKR HFL. Panels (a)-(b): distribution of the fitted  
 391 normalized amplitude of the relative SKR HFL in the north and south as a function of the local time and  
 392 latitude (amplitude is normalized by the root mean square deviation:  $A/\text{RMSD}$ ,  $A$  is the amplitude of the  
 393 fitted sinusoidal function,  $\text{RMSD}$  is the calculated root mean square deviation, see more details in  
 394 Appendix). Panels (c)-(d): same format as the Panels (a)-(b) but for the fitted phase ( $\varphi$  of the sinusoidal  
 395 function). The bin size of Panels (a)-(d) is  $[4^\circ \text{ Lat} \times 2 \text{ hours LT}]$  and the  $\text{RMSD}$  threshold used to discard  
 396 the poor fits is 0.1. Panel (e): local time slice of the sinusoidal fits of the modulation of the north SKR  
 397 HFL. The fitted sinusoidal curves in each local time bin are displayed at  $\text{Lat} = [16^\circ \text{ } 20^\circ]$  and at  $\text{Lat}$   
 398  $= [-22^\circ \text{ } -18^\circ]$  for the southern hemisphere in Panel (f). The plotted curves are normalized in amplitude.  
 399 The real amplitude of each modulation is indicated near the ticks to the left. The red boxes mark the local  
 400 times where the stronger modulation and relative stable phase of the sinusoidal fits are observed, and the  
 401 corresponding SLS5 ranges of the maxima ( $\text{SLS5N}=[20^\circ \text{ } 115^\circ]$ ,  $\text{SLS5S}=[5^\circ \text{ } 110^\circ]$  for the left-hand side  
 402 red boxes in both Panels (e) and (f) and minima ( $\text{SLS5N}=[220^\circ \text{ } 300^\circ]$ ,  $\text{SLS5S}=[170^\circ \text{ } 260^\circ]$  for the  
 403 right-hand side boxes). The black stars for each curve mark the maxima and minima of the sinusoidal  
 404 functions.

405 Case studies and statistical direction-finding analyses using Cassini data suggested that SKR  
 406 sources are distributed at all longitudes along the magnetic field lines mapping to the UV auroral oval,  
 407 whereas the intensities of SKR maxima are in the morning LT (Ceconi et al., 2009, Lamy et al., 2009,  
 408 2011). It has also been known for long that the SKR intensity modulation is best observed in the morning  
 409 sector (Lamy et al., 2009; Ye et al., 2016; 2018). Therefore, it is interesting to explore further the features  
 410 of the modulation, i.e., at which place the modulation is stronger? The distribution of the modulation  
 411 amplitude (with  $A$  the amplitude of the fitted sinusoidal function) and phase ( $\varphi$ ) of the sinusoidal fit for  
 412 each spatial bin is then color-plotted as a function of local time and latitude in Figure 6 Panels (a)-(b).  
 413 The blank bins are due to the lack of data and poor fits. The modulation of relative HFL can be observed

414 in most of the spatial bins as shown by Panels (a)-(b) but with some asymmetries with respect to the  
 415 latitude and LT.

416 Strong modulation in both north and south is observed at  $abs(Lat) \geq 10^\circ$ . The modulation  
 417 amplitude is stronger in the north than in the south. The weaker modulation amplitude observed at  
 418  $-10^\circ \leq Lat \leq 10^\circ$  could be due to the beaming geometry of SKR, as the superposition of SKR from the  
 419 two hemispheres near the equatorial plane may affect the HFL, or may be simply due to the strongly  
 420 modulated source regions not being visible in these low latitude regions. The phases in Panels (c)-(d) ( $\varphi$   
 421 of the sinusoidal functions,  $\varphi \sim 0^\circ$  implies that  $A * \sin(\lambda_{sun} + \varphi)$  function peaks at  $\lambda_{sun} \sim 90^\circ$ ) of  
 422 these regions with strong modulation amplitudes are clustered and show small phases around zero.

423 In Panel (a) of Figure 6, a region exhibiting weaker modulation and scattered phases can be  
 424 observed in the morning side LT, e.g., from 5:00 to 10:00 LT. The cause of this phenomenon may be  
 425 attributed to the shorter observation time in these local times, as suggested in Figure A1 Panels (a)-(b), or  
 426 it could be due to the merging of signals from numerous intense morning side sources that are  
 427 continuously distributed throughout the morning sector and continuously illuminate the nearby region at  
 428 different phases of their modulation. This may result in difficulties for recognizing the modulation  
 429 features in these bins, as suggested by the large RMSD (poor sinusoidal fits) shown in Figure A1 Panels  
 430 (b) and (d). Additionally, the modulation also appears weaker from 20:00 to 22:00 LT. Weakly  
 431 modulated signal from the nearby LT to the 20:00 to 22:00 sector may result in weak modulations seen  
 432 there.

433 To give an intuitive illustration of the relative HFL modulation at different LT bins, the fitted  
 434 sinusoidal curves at  $Lat = [16^\circ, 20^\circ]$  in the northern hemisphere are shown in Panel (e) (the 24 sub-panels  
 435 for different local times are normalized in the vertical direction to address the phase relation, the real (or  
 436 "physical") amplitude of each curve is indicated near the ticks to the left). The red boxes mark the local  
 437 time intervals where the stronger modulation and relative stable phase of the sinusoidal fits are  
 438 consistently observed. The black stars for each curve mark the maxima and minima of the sinusoidal  
 439 functions. As shown by Figure 6 Panel (e), the curves with larger amplitude mostly show similar  
 440 modulation phases, e.g., indicated by the red box with  $LT=11\sim 19$  and  $LT=0\sim 4$ , whereas the curves with  
 441 smaller amplitude show dispersed phases, e.g.,  $LT=5\sim 10$  and  $LT=20\sim 23$ , which could be related to the  
 442 shorter observation time in the corresponding bins and poor fits caused by the strong modulated morning  
 443 side SKR sources. The southern modulation pattern has similar features, as shown in Panel (f), for a  
 444 latitudinal slice at  $Lat = [-22^\circ, -18^\circ]$ . The choice of the two latitude slices in Panels (e)-(f) is because  
 445 these latitudes cover most of the local times as can be seen in Figure 6 Panels (a)-(b), as the other  
 446 latitudes have more blank bins due to poor fits or lack of data.

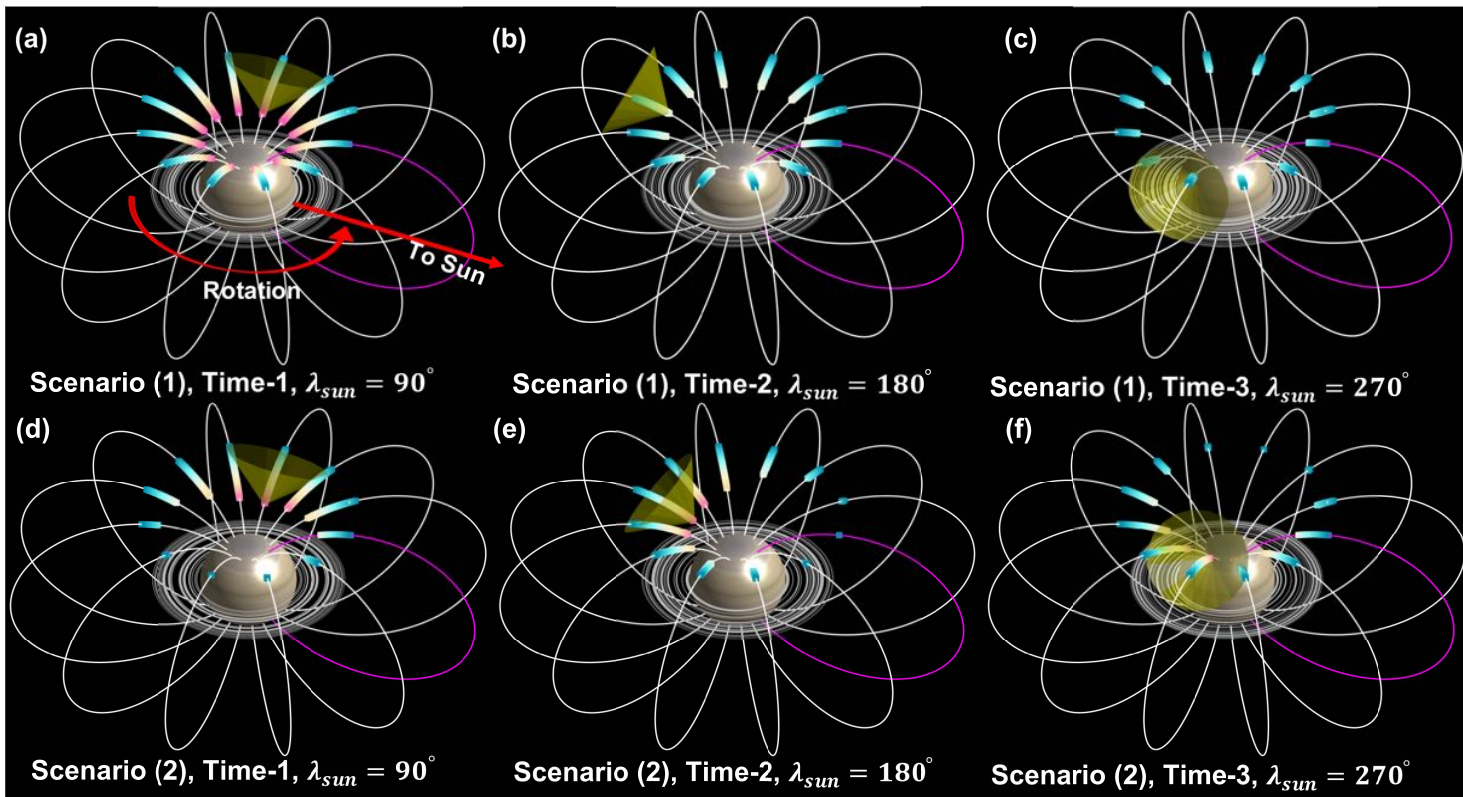
## 447 7. Simulation of the SKR visibility

448 To explain the relative HFL modulations observed in Sections 5-6, simple simulations have been  
 449 carried out using a dipole field with a magnetic moment of 0.21 Gauss and an empirical beaming angle  
 450 derived from data in a previous work (adopted from the black dashed line in Figure 9 of Lamy et al.,  
 451 2013). The wave frequencies are assumed to be equal to the local  $f_{ce}$ . The SKR sources can be distributed  
 452 on a set of Lshells of given longitudes, at altitudes corresponding to the emitted frequencies. The SKR  
 453 spectrogram seen by an observer at a given LT and latitude is obtained by calculating the angles between  
 454 the location of the observer and the magnetic field vector in SKR sources at each frequency / Lshell / LT  
 455 / longitude. The frequencies for which these angles match the emission beaming cone are visible for the  
 456 observer, the others are not. The thickness of the hollow cone wall is set to be  $5^\circ$  in our simulation  
 457 (Lamy et al., 2013). For one set of given SKR sources, the SKR visibility spectrogram during 1 Saturn

458 rotation is derived by combining the calculations for sources at each time step (corresponding to a  
 459 specific sub-solar longitude) and noting the highest visible frequency. We set the  $0^\circ$  sub-solar longitude  
 460 at 12:00 LT to be the first time-step at the start of each calculation.

461 The relative HFL modulation vs sub-solar longitude observed at certain locations could be  
 462 generated by either a temporal effect (e.g., a variation in source altitudes generated, e.g., by periodic  
 463 electron precipitation) or a spatial effect (effects related to the rotation of the planet, e.g., the existence of  
 464 a complex source structure could produce the HFL variation as the planet is rotating), or both.

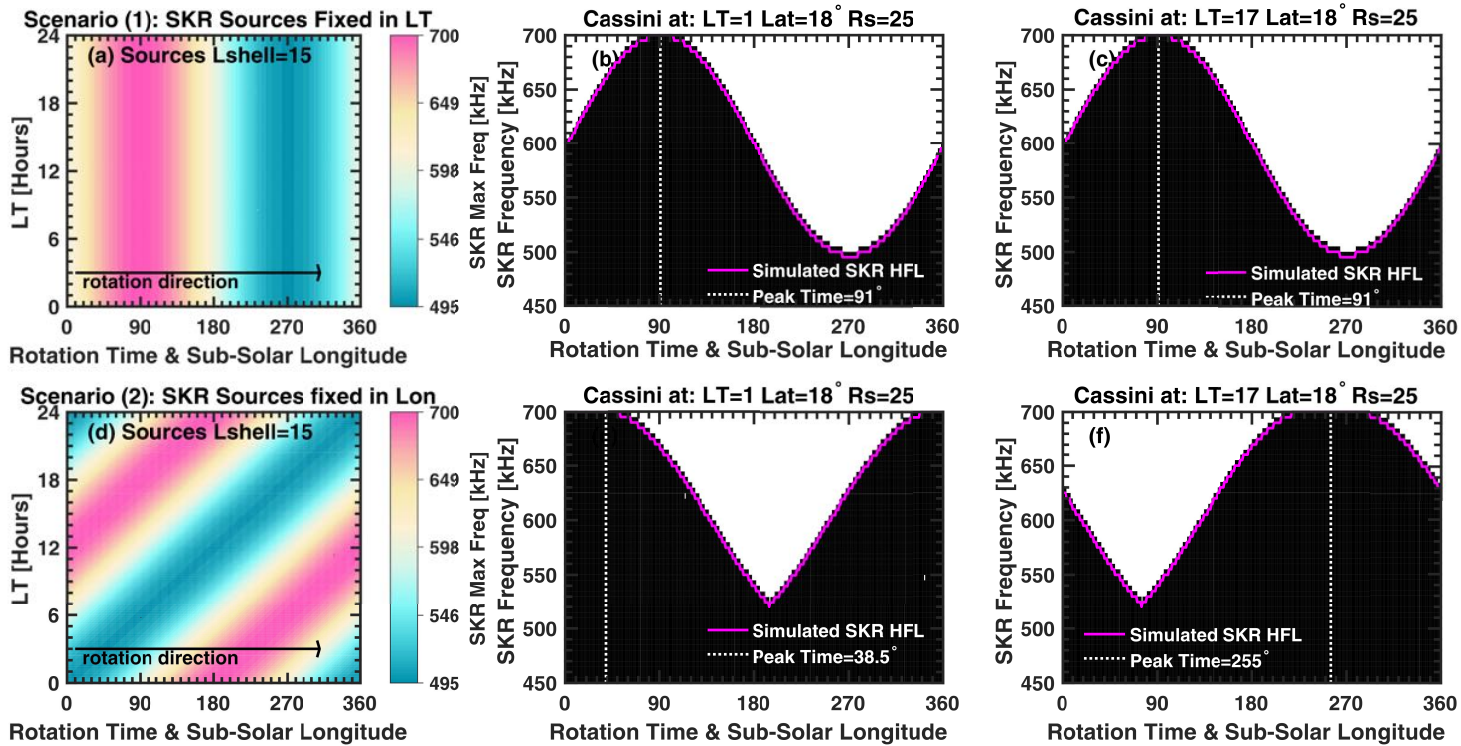
465 To keep the analysis simple, two scenarios were considered: (1) temporal effect: the SKR source  
 466 is fixed in LT and the source frequencies (altitudes) are changing with time, or equivalently with rotation,  
 467 as long thought from Voyager results (Warwick et al., 1981). (2) spatial effect: the SKR sources are  
 468 located at certain longitudes and frequencies (at fixed altitudes, frequencies do not change with time) and  
 469 the sources corotate with the planet, as evidenced by Cassini measurements (Lamy et al., 2009; Cecconi  
 470 et al., 2009; Andrews et al., 2011).



471  
 472 **Figure 7.** Cartoon illustration of the source configuration for the two Scenarios. Panel (a) displays Saturn  
 473 with a dipole magnetic field with the SKR sources distributed in the north polar region. The pink  
 474 magnetic field line is at the sub-solar longitude (LT=12:00,  $\lambda_{sun} = 90^\circ$ ). The cyan-red markers show the  
 475 SKR source configuration in the simulation of Scenario (1). The yellow transparent cone is an example  
 476 of the SKR beaming. The beaming cone is at  $\lambda_{sun} = 90^\circ$  in Panel (a) and it rotates to  $\lambda_{sun} = 180^\circ$  and  
 477  $\lambda_{sun} = 270^\circ$  in Panels (b)-(c). Panels (a)-(c) give the distribution of SKR sources at different simulation  
 478 time steps. Panels (d)-(f) give the configurations of SKR sources for Scenario (2). Note that the “Time-1”  
 479 in Panels (a)-(b) with  $\lambda_{sun} = 90^\circ$  is arbitrarily chosen to mark the time coordinate, which is different  
 480 from the time-step 1 in the simulation that starts from  $\lambda_{sun} = 0^\circ$ .

481 In scenario (1), we only assume that the SKR sources are varying sinusoidally in frequency as a  
 482 function of time because the observed HFL does so. If identical SKR sources are placed at all longitudes  
 483 and they change together in frequency with a sinusoidal pattern as a function of time, the observer will  
 484 naturally observe a sinusoidal HFL variation at the same phase at all LT (the observer's latitude being  
 485 fixed) as illustrated in Figure 7 Panels (a)-(c).

486 In scenario (2), the complicated source structure could be constructed by simply setting the SKR  
 487 sources to all longitudes and by giving a different maximum frequency at each longitude, as shown in  
 488 Figure 7 Panels (d)-(f). As one can imagine, in this case, an observer at a fixed location will thus intersect  
 489 the hollow cones at different frequencies as the planet rotates, and thus see a changing HFL.



490  
 491 **Figure 8.** Simulation of the SKR HFL modulations. Panel (a) displays Test 1 for Scenario (1), the SKR  
 492 sources are fixed in LT range [0:00 -24:00] at Lshell=15. The maximum SKR frequencies are indicated  
 493 in color code and all the source frequencies are changing together sinusoidally as a function of time /  
 494 sub-solar longitude. Panels (b)-(c) display the SKR HFL modulations for different observer's locations  
 495 under the conditions of Scenario (1). Cassini at LT= 01:00, Lat = 18° and Rs=25 Saturn radii in Panel (b)  
 496 and similar location but at LT=17:00 for Panel (c). Panel (d) displays the source configuration of  
 497 Scenario (2), the SKR sources are placed at all longitudes. The maximum frequencies of SKR at different  
 498 longitudes are different and do not change with time. Panels (e)-(f) display SKR visibility spectrograms  
 499 for different observer's locations (same as Panels (b)-(c)) under the conditions of Scenario (2).

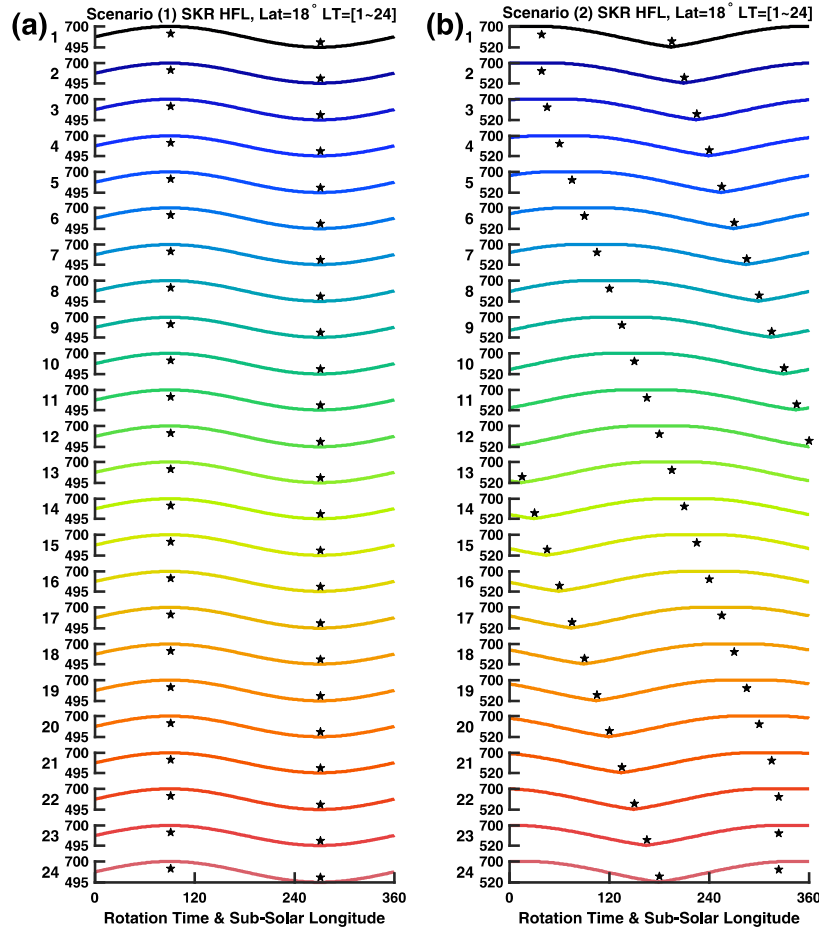
500 The simulation results are given in Figure 8. For Scenario (1), the LT view of the maximum SKR  
 501 frequency distribution as a function of time is quantitatively given in Figure 8 Panel (a). All these sources  
 502 are changing sinusoidally together as a function of time as shown by the color code (only the maximum  
 503 frequency along each field line is plotted). We arbitrarily distributed the SKR sources between 400 kHz  
 504 to 700 kHz (step = 5 kHz) at Lshell=15, but taking another range does not change the shape of the results.  
 505 A sinusoidal variation of the HFL is obtained as indicated by the pink lines in Panels (b)-(c). At any two

506 different local times, i.e., 01:00 for Panel (b) and 17:00 for Panel (c), the HFL peak times are identical  
 507 and at time step 92, i.e., when the sub-solar longitude reaches  $91^\circ$ .

508 For Scenario (2), we set the SKR sources along  $L=15$  field lines at all longitudes ( $1^\circ$ - $360^\circ$ ,  
 509 step= $1^\circ$ ), from 400 kHz to 700 kHz (step = 5 kHz). Then we applied a sinusoidal variation to the  
 510 frequency range of SKR sources as a function of the longitude as can be seen in Panels (d) in Figure 8.  
 511 The maximum frequency at each longitude as a function of rotating time is quantitatively given in Figure  
 512 8 Panel (d). The color code in Panel (d) suggests that the maximum frequency of a longitude-fixed  
 513 rotating source produces a complicated pattern in view of a fixed observer at a certain LT and as a  
 514 function of time. Clear sinusoidal (or quasi-sinusoidal) variations in the HFL are observed in Figure 8  
 515 Panels (e)-(f), which is calculated using the source configuration in Figure 8 Panel (d). The observers at  
 516 different LT observe different phases with the HFL peaking at  $38.5^\circ$  in Panel (e) and  $255^\circ$  in Panel (f),  
 517 which is similar to the small phase shifts as observed in Figure 6 Panels (e)-(f).

518

519



520

521

522

523 **Figure 9.** Simulated northern HFL modulation at  $\text{Lat} = 18^\circ$  and different LTs. Format is similar to  
 524 Figure 6 Panel (e). Panel (a) displays the results of the scenario (1) simulation (LT-fixed but

525 time-variable sources). Panel (b) displays the results of the scenario (2) simulation (Longitude-fixed,  
526 rotating sources).

527 The simulation results at  $\text{Lat} = 18^\circ$  and different LTs are given in Figure 9 in the same format as  
528 Figure 6 Panels (e)-(f) (at the same latitude with  $\text{Lat} = 18^\circ$ ). The results of Scenario (1) simulation are  
529 shown in Figure 9 Panel (a). At all LTs where the SKR is visible, the observed HFL change together with  
530 no phase shifts. Results of Scenario (2) simulation displayed in Panel (b) are similar to the results in  
531 Panel (a) but with a shift at each LT. These shifts are introduced by the rotation of the planet as shown in  
532 Figure 8 Panel (d).

533 A combination of both scenarios is needed to explain the observations. Scenario (1) provides  
534 modulations in HFL with stable phases, and scenario (2) provides intermittent small phase shifts. The  
535 maxima and minima of the obtained sinusoidal curves are mostly concentrated at fixed longitudes as  
536 indicated by the red boxes in Figure 6 Panels (e)-(f) and only small phase shifts are observed, which are  
537 possibly generated by the rotation of the source region as suggested by Scenario (2) simulation.  
538 Therefore, the sinusoidal modulation phenomenon of the relative SKR HFL could be generated by the  
539 combination of the two simulated situations, that is, the SKR sources corotate with the planet, but many  
540 of them show a strong time-variation and may be fixed in local time.

## 541 8. Discussion and Summary

542 The initial understanding of the SKR is a “clock” like source, which means that the SKR sources  
543 are fixed in LT and change emission characteristics (intensity, HFL) as a function of time or sub-solar  
544 longitude (Warwick et al., 1981; corresponding to Scenario (1) simulation in the last Section), whereas  
545 later studies show that the SKR sources also behave as a rotating beam that corotates with the planet and  
546 goes over all longitudes with time, along a circumpolar oval whose intensity peaks at dawn (Lamy et al.,  
547 2009; Cecconi et al., 2009; Andrews et al., 2011; similar to Scenario (2) simulations). Hence the  
548 modulation of SKR tends to be a combination of the temporal and spatial effects, as shown by Cassini  
549 radio direction-finding and magnetic measurements (Lamy, 2011, Andrews et al., 2011) and modeled in  
550 our Scenarios. The same is found for the relative HFL modulation studied in this work.

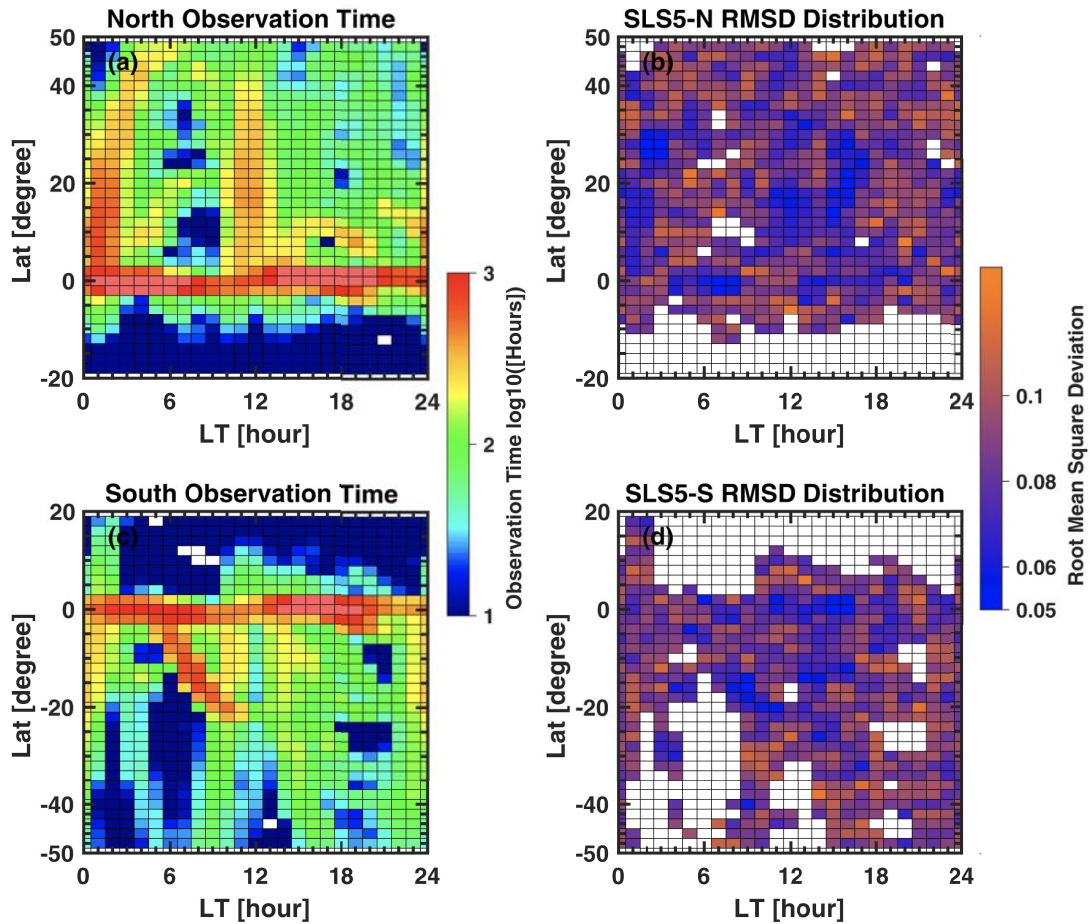
551 The source altitudes of the SKR rely on both the CMI conditions (i.e.,  $f_{pe}/f_{ce}$ ) and the electron  
552 distribution (Wu & Lee, 1979; Lamy et al., 2009, 2018). The CMI condition is not likely to cause the  
553 source altitude variation because the plasma density at the SKR source region is mainly related to the  
554 ionospheric plasma density, which decays exponentially. The  $\sim 1$  rotation period modulation of relative  
555 HFL can be observed both on the dayside and on the nightside, which suggests the ionospheric  
556 conductance does not play a major role in producing the modulation. Hence the formation of the  
557 shell-like electron distribution is a likely reason for the modulation of the source altitudes, which is  
558 further related to particle transport and associated current systems. The corotating source structure could  
559 be formed naturally because electron precipitation is different at different longitudes, leading to the  
560 formation of complex source regions. Further details to understand the SKR source variations would  
561 require simulations of the electron precipitation, forming of the field-aligned currents and calculation of  
562 the wave growth rate, which are beyond the scope of this work.

563 The previous work of Galopeau, Ortega-Molina, and Zarka, (1991) analyzed Voyager-Saturn  
564 data for 3-4 months around each fly-by to study the SKR HFL. Because the fly-bys of the Voyager  
565 spacecraft only covered limited local time and latitude ranges, these authors also observed a sinusoidal  
566 variation of the relative HFL as a function of sub-solar longitude. Their explanation of this variation in  
567 terms of a magnetic field anomaly was a logical one (that can be reproduced by our simulations). More  
568 than 40 years after the Voyager Saturn fly-bys in 1980 & 1981, having Cassini observations at all LT and

569 latitudes, having discovered the SLS5 system with variable N & S periods, having checked that no single  
 570 rigid rotation period can explain the observed relative HFL modulations better than SLS5, and having the  
 571 direct calculation of the HFL modulation spectrograms, we can conclude that this modulation is related  
 572 to the SKR current systems and refute the need for a magnetic anomaly.

573 This present work makes it possible to obtain all the SKR HFL during the 13 years of Cassini's  
 574 orbital tour around Saturn by using an automatic detection algorithm. The characteristics of HFL are  
 575 analyzed. The average HFL in the northern hemisphere is at 625 kHz, and at 539 kHz in the south. The  
 576 difference in the average frequency between the two hemispheres is produced by the northward offset of  
 577 the Saturnian magnetic field. The SKR HFL can cover almost all the regions in the vicinity of Saturn as  
 578 seen in the quite uniform distribution of HFL. Sinusoidal modulation of the relative SKR HFL is  
 579 observed when the data are restricted to small spatial bins and organized as a function of sub-solar  
 580 longitude. The LSSA calculation using the relative HFL time series directly confirms the modulation of  
 581 relative HFL at the SLS5 modulation periods and hence excludes the possibility of the existence of a  
 582 magnetic anomaly. Simulation results suggest that the modulation could be explained by a rotating SKR  
 583 source superimposed with a strong temporal modulation, which is consistent with the previous studies.  
 584 The source structure and the variation could be related to the electron precipitation processes in the SKR  
 585 source regions, and this may be covered in a future study.

## 586 Appendix



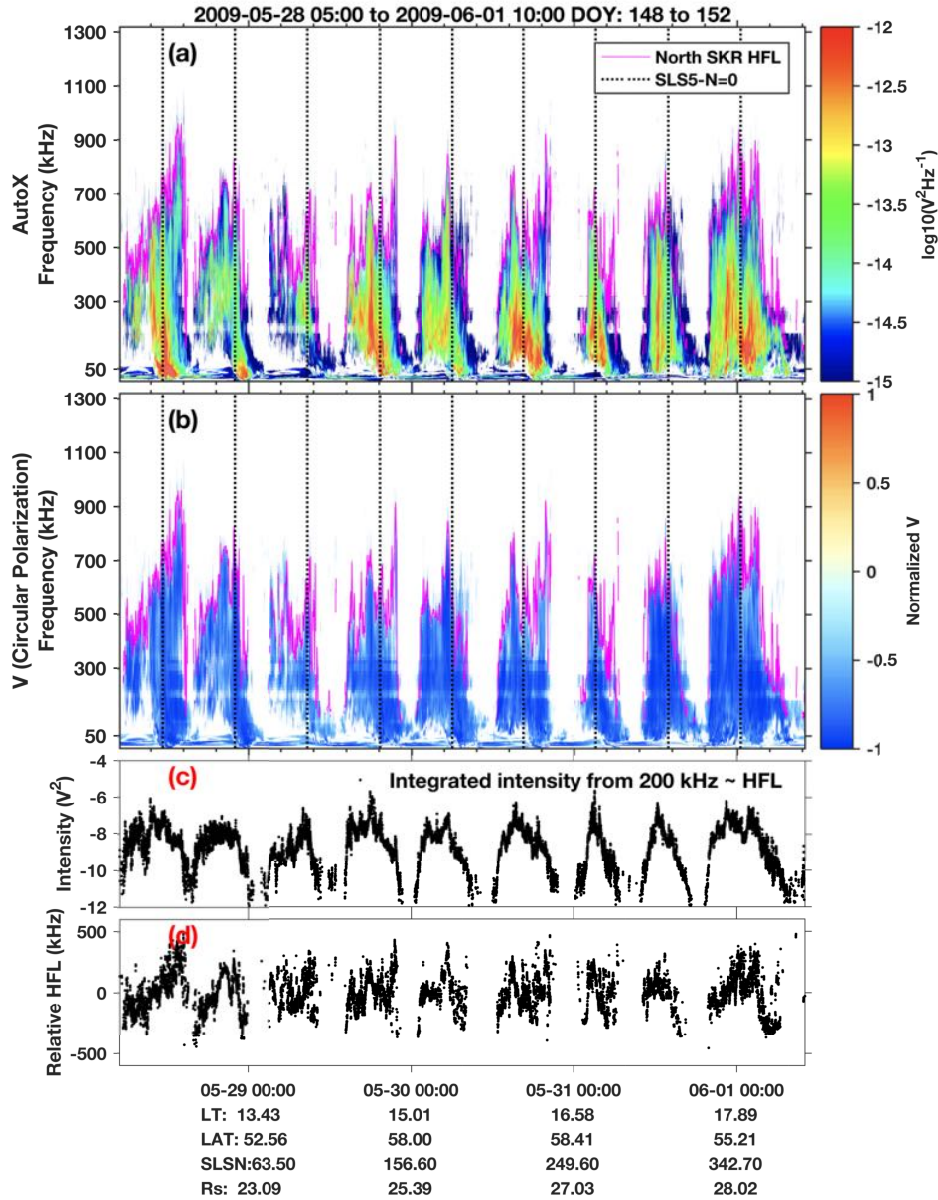
587

588 **Figure A1.** Observation time and the RMSD in each of the spatial bins. Panel (a) gives the observation  
 589 time of Cassini in each spatial bin when the north HFL is observed. Panel (b) give the calculated RMSD  
 590 for the sinusoidal fits of the relative HFL with respect to the SLS5 longitude when using SLS5-N. Panels  
 591 (c)-(d) give the results in the same format as Panels (a)-(b) but for the southern hemisphere.

592 The observation time and the calculated RMSD of the sinusoidal fits are given in Figure A1. The  
 593 calculated results of the spatial bins shown in Figure 6 Panels (a)-(b) have to satisfy two criteria: (1) data  
 594 inside each bin must have an observation time larger than 3 rotation periods (1 Saturn rotation time  $\cong$   
 595 10.6 hours); (2) The RMSD value is less than 0.1 (roughly 40% of all the bins exhibit RMSD >0.1).

596 RMSD defined as:  $\sqrt{\frac{1}{n} \sum_{i=1}^n (A * \sin(\text{longitude}(i) + \varphi) - \text{mean}_{hfl}(\text{longitude}(i)))^2}$ , n is the number  
 597 of the data points in the fitting. Here n=90 since we use a longitude step =  $4^\circ$ . A and  $\varphi$  are the amplitude  
 598 and phase obtained by the fittings, respectively. As can be seen from the comparison between the  
 599 calculated RMSD in Figure A1 Panels (b) and (d) and the modulation amplitude in Figure 6 Panels  
 600 (a)-(b), the fitted bins with smaller RMSD also show a stronger modulation amplitude in general. The  
 601 poorly-fitted bins with larger RMSD usually show rather random patterns, so that their removal does not  
 602 affect the results.





603

604 **Figure A2.** Modulation of SKR intensity and HFL. Panel (a) presents the RPWS electric field intensity  
 605 spectrogram, processed using the same methodology as Panels (c)-(d) in Figure 1. Panel (b) displays the  
 606 circular polarization (n3d level data). The overlapping pink line represents the identified SKR HFL. The  
 607 black dotted lines indicate the instances when SLS5-N reaches zero. Panel (c) gives the integrated SKR  
 608 intensity (integrated from 200 kHz to HFL) using the data in Panel (a). Panel (d) gives the relative HFL  
 609 values derived from the pink lines above and by subtracting out the 10.6 hours running average values.

610 Figure A2 demonstrates the modulated occurrence of SKR as seen by a distant observer. A linear  
 611 frequency axis (y-axis) is used to emphasize the HFL variations. The origin of the SKR emissions in  
 612 Figure A2 is in the northern hemisphere, as indicated by the negative polarization values in Panel (b) and  
 613 the associated latitudes below. The black dotted lines indicate the points where SLS5-N reaches 0 degree,  
 614 which closely align with consecutive peaks in SKR intensity. The pink lines on top of the SKR emission,

615 as well as the SKR intensity (in Panel (c)) and relative HFL (in Panel (d)), indicate that the HFL &  
616 relative HFL also experience a modulation that mirrors the repetition of the SKR emission peaks.

## 617 **Acknowledgments**

618 This work was supported by the Strategic Priority Research Program of the Chinese Academy of  
619 Sciences (grant No. XDB 41000000). SYW is also supported by China Scholarship Council. PZ, LL and  
620 BC acknowledge support from the PNP and PNST programs from CNRS/INSU, and from the CNES.  
621 CKL's work at the Dublin Institute for Advanced Studies was funded by the Science Foundation Ireland  
622 Grant 18/FRL/6199. SYW thanks for the helpful discussion of Mingzhe Liu and Zhongying Lu on this  
623 work.

## 624 **Open Research**

625 The Cassini RPWS data used in this work were downloaded from the LESIA/Kronos collection of n2  
626 level (Cecconi, Lamy, and Zarka, 2017c), n3d level (Cecconi, Lamy, and Zarka, 2017a), n3e level  
627 (Cecconi, Lamy, and Zarka, 2017b) (goniopolarimetric inversion results obtained following the method  
628 of Cecconi & Zarka, 2005). The derived SKR HFL data is also available from MASER service via a doi  
629 link: (<https://doi.org/10.25935/dz99-s514> ).

## 630 **References**

- 631 Andrews, D. J., Cecconi, B., Cowley, S. W. H., Dougherty, M. K., Lamy, L., Provan, G., & Zarka, P.  
632 (2011). Planetary period oscillations in Saturn's magnetosphere: Evidence in magnetic field  
633 phase data for rotational modulation of Saturn kilometric radiation emissions. *Journal of*  
634 *Geophysical Research: Space Physics*, 116(A9).  
635 <https://doi.org/https://doi.org/10.1029/2011JA016636>
- 636 Bunce, E. J., Cowley, S. W. H., Wright, D. M., Coates, A. J., Dougherty, M. K., Krupp, N., et al. (2005).  
637 In situ observations of a solar wind compression-induced hot plasma injection in Saturn's tail.  
638 *Geophysical Research Letters*, 32(20). <https://doi.org/https://doi.org/10.1029/2005GL022888>
- 639 Cao, H., Dougherty, M. K., Hunt, G. J., Provan, G., Cowley, S. W. H., Bunce, E. J., et al. (2020). The  
640 landscape of Saturn's internal magnetic field from the Cassini Grand Finale. *Icarus*, 344, 113541.  
641 <https://doi.org/https://doi.org/10.1016/j.icarus.2019.113541>
- 642 Cao, H., Russell, C. T., Christensen, U. R., Dougherty, M. K., & Burton, M. E. (2011). Saturn's very  
643 axisymmetric magnetic field: No detectable secular variation or tilt. *Earth and Planetary Science*  
644 *Letters*, 304(1), 22–28. <https://doi.org/https://doi.org/10.1016/j.epsl.2011.02.035>
- 645 Cecconi, B., Lamy, L., Zarka, P., Prangé, R., Kurth, W. S., & Louarn, P. (2009). Goniopolarimetric study  
646 of the revolution 29 perikrone using the Cassini Radio and Plasma Wave Science instrument  
647 high-frequency radio receiver. *Journal of Geophysical Research: Space Physics*, 114(A3).  
648 <https://doi.org/https://doi.org/10.1029/2008JA013830>
- 649 Cecconi, B., & Zarka, P. (2005). Direction finding and antenna calibration through analytical inversion  
650 of radio measurements performed using a system of two or three electric dipole antennas on a  
651 three-axis stabilized spacecraft. *Radio Science*, 40(3), 1–20.  
652 <https://doi.org/10.1029/2004RS003070>
- 653 Cecconi, B., Lamy, L., & Zarka, P. (2017a). Cassini/RPWS/HFR LESIA/Kronos N3d Data Collection  
654 (Version 1.0) [Data set]. PADC. <https://doi.org/10.25935/5JFX-DH49>

- 655 Cecconi, B., Lamy, L., & Zarka, P. (2017b). Cassini/RPWS/HFR LESIA/Kronos N3e Data Collection  
656 (Version 1.0) [Data set]. PADC. <https://doi.org/10.25935/9ZAB-FP47>
- 657 Cecconi, B., Lamy, L., & Zarka, P. (2017c). Cassini/RPWS/HFR LESIA/Kronos N2 Data Collection  
658 (Version 1.0) [Data set]. PADC. <https://doi.org/10.25935/XS9J-ND90>
- 659 Cowley, S. W. H. & Provan, G. Planetary period modulations of Saturn’s magnetotail current sheet  
660 during northern spring: Observations and modeling. *J. Geophys. Res. Sp. Phys.* 122, 6049–6077  
661 (2017).
- 662 Cowley, S. W. H., & Provan, G. (2016). Planetary period oscillations in Saturn’s magnetosphere: Further  
663 comments on the relationship between post-equinox properties deduced from magnetic field and  
664 Saturn kilometric radiation measurements. *Icarus*, 272, 258–276.  
665 <https://doi.org/https://doi.org/10.1016/j.icarus.2016.02.051>
- 666 Desch, M. D., & Rucker, H. O. (1983). The relationship between Saturn kilometric radiation and the  
667 solar wind. *Journal of Geophysical Research: Space Physics*, 88(A11), 8999–9006.  
668 <https://doi.org/https://doi.org/10.1029/JA088iA11p08999>
- 669 Desch, M. D. (1982). Evidence for solar wind control of saturn radio emission. *Journal of Geophysical*  
670 *Research: Space Physics*, 87(A6), 4549–4554.  
671 <https://doi.org/https://doi.org/10.1029/JA087iA06p04549>
- 672 Dougherty, M. K., Cao, H., Khurana, K. K., Hunt, G. J., Provan, G., Kellock, S., et al. (2018). Saturn’s  
673 magnetic field revealed by the Cassini Grand Finale. *Science*, 362(6410), eaat5434.  
674 <https://doi.org/10.1126/science.aat5434>
- 675 Farrell, W. M., Desch, M. D., Kaiser, M. L., Lecacheux, A., Kurth, W. S., Gurnett, D. A., et al. (2005). A  
676 nightside source of Saturn’s kilometric radiation: Evidence for an inner magnetosphere energy  
677 driver. *Geophysical Research Letters*, 32(18).  
678 <https://doi.org/https://doi.org/10.1029/2005GL023449>
- 679 Fischer, G., Cecconi, B., Lamy, L., Ye, S.-Y., Taubenschuss, U., Macher, W., et al. (2009). Elliptical  
680 polarization of Saturn Kilometric Radiation observed from high latitudes. *Journal of Geophysical*  
681 *Research: Space Physics*, 114(A8). <https://doi.org/https://doi.org/10.1029/2009JA014176>
- 682 Fischer, G., Gurnett, D. A., Kurth, W. S., Ye, S.-Y., & Groene, J. B. (2015). Saturn kilometric radiation  
683 periodicity after equinox. *Icarus*, 254, 72–91.  
684 <https://doi.org/https://doi.org/10.1016/j.icarus.2015.03.014>
- 685 Galopecau, P., Ortega-Molina, A., & Zarka, P. (1991). Evidence of Saturn’s magnetic field anomaly from  
686 Saturnian kilometric radiation high-frequency limit. *Journal of Geophysical Research*, 96(A8),  
687 14129–14140. <https://doi.org/10.1029/91JA00696>
- 688 Galopecau, P., & Zarka, P. (1992). Reply [to “Comment on ‘Evidence of Saturn’s magnetic field anomaly  
689 from saturnian kilometric radiation high-frequency limit’”]. *Journal of Geophysical Research:*  
690 *Space Physics*, 97(A8), 12291–12297. <https://doi.org/https://doi.org/10.1029/92JA00323>
- 691 Gurnett, D. A., Kurth, W. S., Kirchner, D. L., Hospodarsky, G. B., Averkamp, T. F., Zarka, P., et al.  
692 (2004). The Cassini Radio and Plasma Wave Investigation. *Space Science Reviews*, 114(1), 395–  
693 463. <https://doi.org/10.1007/s11214-004-1434-0>
- 694 Gurnett, D. A., Persoon, A. M., Groene, J. B., Kopf, A. J., Hospodarsky, G. B., & Kurth, W. S. (2009). A  
695 north-south difference in the rotation rate of auroral hiss at Saturn: Comparison to Saturn’s

- 696           kilometric radio emission. *Geophysical Research Letters*, 36(21).  
 697           <https://doi.org/https://doi.org/10.1029/2009GL040774>
- 698    Hunt, G. J., Cowley, S. W. H., Provan, G., Bunce, E. J., Alexeev, I. I., Belenkaya, E. S., et al. (2015).  
 699           Field-aligned currents in Saturn’s northern nightside magnetosphere: Evidence for  
 700           interhemispheric current flow associated with planetary period oscillations. *Journal of*  
 701           *Geophysical Research: Space Physics*, 120(9), 7552–7584.  
 702           <https://doi.org/https://doi.org/10.1002/2015JA021454>
- 703    Jackman, C. M., & Arridge, C. S. (2011). Statistical properties of the magnetic field in the Kronian  
 704           magnetotail lobes and current sheet. *Journal of Geophysical Research: Space Physics*, 116(A5).  
 705           <https://doi.org/https://doi.org/10.1029/2010JA015973>
- 706    Jackman, C. M., Arridge, C. S., Slavin, J. A., Milan, S. E., Lamy, L., Dougherty, M. K., & Coates, A. J.  
 707           (2010). In situ observations of the effect of a solar wind compression on Saturn’s magnetotail.  
 708           *Journal of Geophysical Research: Space Physics*, 115(A10).  
 709           <https://doi.org/https://doi.org/10.1029/2010JA015312>
- 710    Jackman, C. M., Lamy, L., Freeman, M. P., Zarka, P., Cecconi, B., Kurth, W. S., et al. (2009). On the  
 711           character and distribution of lower-frequency radio emissions at Saturn and their relationship to  
 712           substorm-like events. *Journal of Geophysical Research: Space Physics*, 114(A8).  
 713           <https://doi.org/https://doi.org/10.1029/2008JA013997>
- 714    Kaiser, M. L., Desch, M. D., Warwick, J. W., & Pearce, J. B. (1980). Voyager detection of nonthermal  
 715           radio emission from Saturn. *Science*, 209(4462), 1238–1240.
- 716    Kaiser, M. L., & Desch, M. D. (1982). Saturnian kilometric radiation: Source locations. *Journal of*  
 717           *Geophysical Research: Space Physics*, 87(A6), 4555–4559.  
 718           <https://doi.org/https://doi.org/10.1029/JA087iA06p04555>
- 719    Kivelson, M. G., & Jia, X. (2018). Coupled SKR Emissions in Saturn’s Northern and Southern  
 720           Ionospheres. *Geophysical Research Letters*, 45(7), 2893–2900.  
 721           <https://doi.org/https://doi.org/10.1002/2017GL075425>
- 722    Kimura, T., Lamy, L., Tao, C., Badman, S. V., Kasahara, S., Cecconi, B., et al. (2013). Long-term  
 723           modulations of Saturn’s auroral radio emissions by the solar wind and seasonal variations  
 724           controlled by the solar ultraviolet flux. *Journal of Geophysical Research: Space Physics*, 118(11),  
 725           7019–7035. <https://doi.org/https://doi.org/10.1002/2013JA018833>
- 726    Kurth, W. S., Gurnett, D. A., Clarke, J. T., Zarka, P., Desch, M. D., Kaiser, M. L., et al. (2005). An  
 727           Earth-like correspondence between Saturn’s auroral features and radio emission. *Nature*,  
 728           433(7027), 722–725. <https://doi.org/10.1038/nature03334>
- 729    Kraus, J. D. (1966). *Radio astronomy* (pp. 116–125). McGraw-Hill.
- 730    Lamy, L. (2017). The Saturnian kilometric radiation before the Cassini Grand Finale. In G. Fischer, G.  
 731           Mann, M. Panchenko, & P. Zarka (Eds.), *Planetary Radio Emissions VIII* (pp. 171–190).  
 732           <https://doi.org/10.1553/PRE8s171>
- 733    Lamy, L., Cecconi, B., Prangé, R., Zarka, P., Nichols, J. D., & Clarke, J. T. (2009). An auroral oval at the  
 734           footprint of Saturn’s kilometric radio sources, colocated with the UV aurorae. *Journal of*  
 735           *Geophysical Research: Space Physics*, 114(A10).  
 736           <https://doi.org/https://doi.org/10.1029/2009JA014401>

- 737 Lamy, L., Prangé, R., Pryor, W., Gustin, J., Badman, S. V., Melin, H., et al. (2013). Multispectral  
 738 simultaneous diagnosis of Saturn's aurorae throughout a planetary rotation. *Journal of*  
 739 *Geophysical Research: Space Physics*, 118(8), 4817–4843.  
 740 <https://doi.org/https://doi.org/10.1002/jgra.50404>
- 741 Lamy, L., Zarka, P., Cecconi, B., Prangé, R., Kurth, W. S., & Gurnett, D. A. (2008a). Saturn kilometric  
 742 radiation: Average and statistical properties. *Journal of Geophysical Research: Space Physics*,  
 743 113(A7). <https://doi.org/https://doi.org/10.1029/2007JA012900>
- 744 Lamy, L., Zarka, P., Cecconi, B., Hess, S., & Prangé, R. (2008b). Modeling of Saturn kilometric  
 745 radiation arcs and equatorial shadow zone. *Journal of Geophysical Research: Space Physics*,  
 746 113(A10). <https://doi.org/https://doi.org/10.1029/2008JA013464>
- 747 Lamy, L., Zarka, P., Cecconi, B., Prangé, R., Kurth, W. S., Hospodarsky, G., et al. (2018). The  
 748 low-frequency source of Saturn's kilometric radiation. *Science*, 362(6410), eaat2027.  
 749 <https://doi.org/10.1126/science.aat2027>
- 750 Lamy, L., Cecconi, B., Zarka, P., Canu, P., Schippers, P., Kurth, W. S., et al. (2011). Emission and  
 751 propagation of Saturn kilometric radiation: Magnetoionic modes, beaming pattern, and  
 752 polarization state. *Journal of Geophysical Research: Space Physics*, 116(4), 1–16.  
 753 <https://doi.org/10.1029/2010JA016195>
- 754 Lamy, L., Schippers, P., Zarka, P., Cecconi, B., Arridge, C. S., Dougherty, M. K., et al. (2010).  
 755 Properties of Saturn kilometric radiation measured within its source region. *Geophysical*  
 756 *Research Letters*, 37(12), 1–6. <https://doi.org/10.1029/2010GL043415>
- 757 McIlwain, C. E. (1966). Magnetic coordinates. *Space Science Reviews*, 5(5), 585–598.  
 758 <https://doi.org/10.1007/BF00167327>
- 759 Menietti, J. D., Mutel, R. L., Schippers, P., Ye, S.-Y., Gurnett, D. A., & Lamy, L. (2011). Analysis of  
 760 Saturn kilometric radiation near a source center. *Journal of Geophysical Research: Space Physics*,  
 761 116(A12). <https://doi.org/https://doi.org/10.1029/2011JA017056>
- 762 Mutel, R. L., Christopher, I. W., & Pickett, J. S. (2008). Cluster multi-spacecraft determination of AKR  
 763 angular beaming. *Geophysical Research Letters*, 35(7), L07104.  
 764 <https://doi.org/https://doi.org/10.1029/2008GL033377>
- 765 Mutel, R. L., Menietti, J. D., Gurnett, D. A., Kurth, W., Schippers, P., Lynch, C., et al. (2010). CMI  
 766 growth rates for Saturnian kilometric radiation. *Geophysical Research Letters*, 37(19).  
 767 <https://doi.org/https://doi.org/10.1029/2010GL044940>
- 768 Provan, G. et al. Planetary Period Oscillations in Saturn's Magnetosphere: Cassini Magnetic Field  
 769 Observations Over the Northern Summer Solstice Interval. *J. Geophys. Res. Sp. Phys.* 123,  
 770 3859–3899 (2018).
- 771 Reed, J. J., Jackman, C. M., Lamy, L., Kurth, W. S., & Whiter, D. K. (2018). Low-Frequency Extensions  
 772 of the Saturn Kilometric Radiation as a Proxy for Magnetospheric Dynamics. *Journal of*  
 773 *Geophysical Research: Space Physics*, 123(1), 443–463. <https://doi.org/10.1002/2017JA024499>
- 774 Southwood, D. J. & Cowley, S. W. H. The origin of Saturn's magnetic periodicities: Northern and  
 775 southern current systems. *J. Geophys. Res. Sp. Phys.* 119, 1563–1571 (2014). doi:  
 776 10.1002/2013JA019632

- 777 Taubenschuss, U., Rucker, H. O., Kurth, W. S., Cecconi, B., Zarka, P., Dougherty, M. K., & Steinberg, J.  
 778 T. (2006). Linear prediction studies for the solar wind and Saturn kilometric radiation. *Annales*  
 779 *Geophysicae*, 24(11), 3139–3150. <https://doi.org/10.5194/angeo-24-3139-2006>
- 780 Treumann, R. A. (2006). The electron–cyclotron maser for astrophysical application. *The Astronomy*  
 781 *and Astrophysics Review*, 13(4), 229–315. <https://doi.org/10.1007/s00159-006-0001-y>
- 782 Warwick, J. W., Pearce, J. B., Evans, D. R., Carr, T. D., Schauble, J. J., Alexander, J. K., et al. (1981).  
 783 Planetary Radio Astronomy Observations from Voyager 1 Near Saturn. *Science*, 212(4491),  
 784 239–243. <https://doi.org/10.1126/science.212.4491.239>
- 785 Wu, C. S., & Lee, L. C. (1979). A theory of the terrestrial kilometric radiation. *The Astrophysical Journal*,  
 786 230(July), 621. <https://doi.org/10.1086/157120>
- 787 Wu, S.Y., Ye, S.Y., Fischer, G., Wang, J., Long, M., Menietti, J. D., et al. (2021). Statistical Study on  
 788 Spatial Distribution and Polarization of Saturn Narrowband Emissions. *The Astrophysical*  
 789 *Journal*, 918(2), 64. <https://doi.org/10.3847/1538-4357/ac0af1>
- 790 Wu, S.Y., Zarka, P., Lamy, L., Taubenschuss, U., Cecconi, B., Ye, S.Y., et al. (2022a). Observations of  
 791 the First Harmonic of Saturn Kilometric Radiation During Cassini’s Grand Finale. *Journal of*  
 792 *Geophysical Research: Space Physics*, 127(9), e2022JA030776.  
 793 <https://doi.org/https://doi.org/10.1029/2022JA030776>
- 794 Wu, S. Y., Ye, S. Y., Fischer, G., Taubenschuss, U., Jackman, C. M., O’Dwyer, E., et al. (2022b). Saturn  
 795 Anomalous Myriametric Radiation, a New Type of Saturn Radio Emission Revealed by Cassini.  
 796 *Geophysical Research Letters*, 49(16), e2022GL099237.  
 797 <https://doi.org/https://doi.org/10.1029/2022GL099237>
- 798 Ye, S.-Y., Fischer, G., Kurth, W. S., Menietti, J. D., & Gurnett, D. A. (2018). An SLS5 Longitude  
 799 System Based on the Rotational Modulation of Saturn Radio Emissions. *Geophysical Research*  
 800 *Letters*, 45(15), 7297–7305. <https://doi.org/https://doi.org/10.1029/2018GL077976>
- 801 Ye, S.-Y., Gurnett, D. A., Fischer, G., Cecconi, B., Menietti, J. D., Kurth, W. S., et al. (2009). Source  
 802 locations of narrowband radio emissions detected at Saturn. *Journal of Geophysical Research:*  
 803 *Space Physics*, 114(A6). <https://doi.org/https://doi.org/10.1029/2008JA013855>
- 804 Ye, S.-Y., Fischer, G., Kurth, W. S., Menietti, J. D., & Gurnett, D. A. (2016). Rotational modulation of  
 805 Saturn’s radio emissions after equinox. *Journal of Geophysical Research: Space Physics*, 121(12),  
 806 11,711–714,728. <https://doi.org/https://doi.org/10.1002/2016JA023281>
- 807 Zarka, P. (1998). Auroral radio emissions at the outer planets: Observations and theories. *Journal of*  
 808 *Geophysical Research: Planets*, 103(E9), 20159–20194.  
 809 <https://doi.org/https://doi.org/10.1029/98JE01323>
- 810 Zarka, P., Lamy, L., Cecconi, B., Prangé, R., & Rucker, H. O. (2007). Modulation of Saturn’s radio clock  
 811 by solar wind speed. *Nature*, 450(7167), 265–267. <https://doi.org/10.1038/nature06237>